# UNIVERSITÀ DEGLI STUDI DI PADOVA

Dipartimento di Fisica e Astronomia “Galileo Galilei”

Master Degree in Nuclear Physics

Final Dissertation

# Study of lifetimes of nuclear excited states near the N=20 island of inversion using the Doppler Shift Attenuation Method

| Thesis supervisors | Candidate |
|---|---|
| Prof. Daniele Mengoni | Raquel Nicolás del Álamo |
| Dr. Franco Galtarossa | |
| Dr. Irene Zanon | |
| Dr. Daniele Brugnara | |

Academic Year 2022 / 2023

# Abstract

In the region along the neutron-rich $N = 20$ shell closure, the ground-state structure of certain isotopes is known to be dominated by intruder configurations. In these configurations, neutrons occupy states above the $N = 20$ shell gap, while leaving vacancies in the shell below. This area on the nuclear chart is known as the $N = 20$ *island of inversion.* The trend extends to nearby nuclei, where sets of intruder states have been found among their excited states.

Lifetime measurements are commonly used to unravel the nature and properties of nuclear states, as they are closely related to transition probabilities. Comparing those to theoretical predictions, indirect information on the nuclear wave-functions can be extracted.

This thesis provides a first-step analysis of an experiment which aims to investigate the interplay between spherical and intruder configurations in the low-lying states of isotopes on the boundary of the $N = 20$ island of inversion, namely $^{34}$Si and $^{35}$P. The AGATA High-Purity Germanium $\gamma$-tracking array was used in coincidence with the PRISMA high-acceptance magnetic spectrometer to detect the $\gamma$ rays emitted in the decay of the states of interest. From the $\gamma$-ray energy spectrum measured, the Doppler Shift Attenuation Method was used to extract the associated lifetimes, expected to lie in the range from 30 to 100 fs.

The analysis involved processing data from both detectors. In order to extract the lifetimes, the shapes of the peaks in the $\gamma$-ray energy spectrum were compared to those produced by a Monte Carlo `GEANT4` simulation, adapted to mimic the experimental conditions. Doing so, it was possible to estimate the lifetime of the first $2^+$ state in $^{36}$S and provide a first preliminary lifetime estimation for the $3/2^+$ state of $^{35}$P.

# Contents

# 1

# Introduction

Atomic nuclei are many-body quantum systems composed of neutrons and protons which are held together by the strong nuclear force [1]. Despite the complexity of such systems, a number of many-body theoretical methods have been developed over time with the aim of accurately reproducing and predicting nuclear properties spanning the nuclear chart.

Out of the various theoretical approaches, the nuclear shell model is particularly noteworthy [2]. Its primary accomplishment lies in its ability to reproduce the *magic numbers*, which refer to specific neutron and proton numbers where nuclei present enhanced stability compared to their neighboring counterparts. Originally developed as an independent particle model, the nuclear shell model has since advanced into a comprehensive many-body computational framework. This extension involves the consideration of multiple particles within the valence shell, which allows for the inclusion of correlations and results in a successful description of a broad range of nuclei and phenomena across the nuclear chart.

In the field of nuclear physics, the term *island of inversion* designates a specific region on the nuclear chart in which intruder states dominate the ground states of the isotopes within that region. These states occur when one or more nucleons within the atomic nucleus do not follow the usual filling pattern of energy levels predicted by the shell model. Instead, they occupy levels expected to lie higher in energy [3]. This phenomenon is predominantly observed in the region of medium-mass and heavy atomic nuclei when the number of nucleons near the magic numbers of 20, 28, and 40 is significantly increased. Intruder states arise due to the effect of the residual interactions among the nucleons in the valence shells and have a significant impact on the spectroscopic and structure properties, decay modes, deformation, and overall nuclear features.

The study of the island of inversion and related phenomena contributes to our understanding of nuclear structure and shell evolution as more nucleons are added to the valence shell. In particular, the region along the $N = 20$ shell closure has gathered significant attention over time. The work herein focuses on the analysis of an experiment aimed at the study of $^{34}$Si and $^{35}$P which are expected to be located in the boundary of the $N = 20$ island of inversion. The aim is to extract spectroscopic information through the measurement of lifetimes of the excited states of $^{34}$Si and $^{35}$P.

## 1.1 Outline of the work

This work is organized as follows:

- This chapter introduces the basic concepts behind the shell model framework [2] and the phenomena in the region around the $N = 20$ island of inversion, which is the subject of the experiment presented. Then, it highlights a few relevant aspects of electromagnetic transitions and lifetime measurements that are essential for understanding the present work.

- Chapter 2 will provide a detailed overview of the features of the AGATA and PRSIMA detectors.

- Following this, Chapter 3 will delve into the data processing procedures within the AGATA+PRISMA setup. This will encompass a comprehensive breakdown of each stage in the data sorting and optimization, from the raw signals to the tracked $\gamma$-ray spectra in coincidence with the ion species of interest.

- Moving forward, Chapter 4 will showcase the various steps required to perform and optimize the `GEANT4` simulation used to extract the lifetime of the states of interest.

- In Chapter 5 the main results of the analysis will be summarized, together with a discussion on the conclusions drawn from this work.

## 1.2 The nuclear shell model

The first successful formulation of the shell model suggested that the nucleon-nucleon interaction can be described in terms of a spherical mean field. This mean-field consists of a central potential $V_0^{(n,p)}(r_i)$, represented by either a harmonic oscillator or a Woods-Saxon potential, and a strong and attractive spin-orbit term [4]:

$$\hat{u}(r_i) = V_0^{(n,p)}(r_i) + V_{SO}(r_i)\left(\hat{l}_i \cdot \hat{s}_i\right). \tag{1.1}$$

To determine the energy levels and the nuclear wave-functions, the shell model requires diagonalizing the one-particle Hamiltonian. The ground-state wave-function is then given by the product of two separate Slater determinants: one for the protons and another one for the neutrons. Each of these Slater determinants is obtained by filling the lowest energy levels resulting from the diagonalization of the nuclear potential. Figure 1.1 presents the typical shell-model level hierarchy.

The formulation mentioned above is now known as the Independent Particle Model (IPM), which can achieve satisfactory results only for a few closed-shell nuclei and single particle (or hole) states [2]. The IPM falls short when the number of protons and neutrons deviates from the magic numbers. In such cases, it becomes essential to incorporate the "residual" two-body interaction, which gives rise to a more advanced framework known as the interacting shell model.

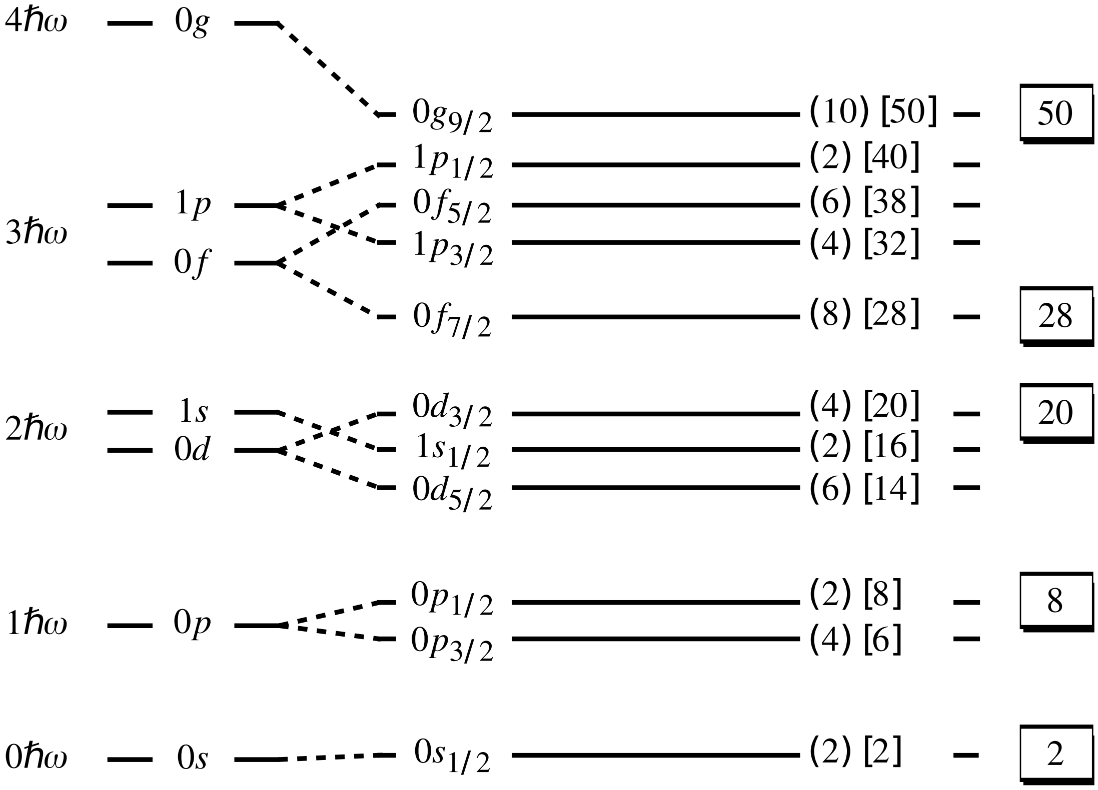

Figure 1.1: Single-particle spectrum showing the contributions coming from the $l \pm \frac{1}{2}$ splitting due to the spin-orbit interaction. The new shell closures, reported on the right, correspond to the magic numbers observed experimentally. Figure taken from [5].

### 1.2.1 The interacting shell model

While the IPM has proven effective in explaining the occurrence of magic numbers in most of the stable atomic nuclei, it is insufficient for describing the nuclear structure throughout the entire nuclear chart. This limitation arises from the crucial influence of residual interactions. To account for the residual interactions, a two-body term is incorporated into the nuclear Hamiltonian:

$$\hat{H} = \hat{H}_0 + \hat{H}_{res} = \sum_{i=1}^{A} \left[ \frac{\hat{p}_i^2}{2m_i} + \hat{u}(r_i) \right] + \frac{1}{2} \sum_{i,j=1}^{A} V_{ij}^{res} \tag{1.2}$$

In the presence of a two-body interaction, the different single-particle configurations $|\Phi\rangle_j$ are mixed. The true eigenvectors, denoted as $|\Psi_k\rangle$, are given by linear combinations of Slater determinants (the set $\{|\Phi\rangle_j\}$ should form a complete basis),

$$|\Psi_k\rangle = \sum_{i=1}^{\infty} C_k^j |\Phi\rangle_j. \tag{1.3}$$

The coefficients $C_k^j$ of the mixing are obtained by diagonalizing the full Hamiltonian including one-body and two-body terms:

$$\hat{H}|\Psi_k\rangle = E_k|\Psi_k\rangle. \tag{1.4}$$

It is important to emphasize that, although the transition from the IPM to the interacting shell model is conceptually simple, practical challenges arise when attempting to diagonalize the nuclear Hamiltonian. The diagonalization techniques impose strong limitations on the maximum matrix dimension that can be computationally handled. The dimension of the Hamiltonian matrix scales as

$$\dim H = \binom{N}{A} = \frac{N!}{A!(N-A)!}, \tag{1.5}$$

where $N$ is the number of single-particle states which the sum in Equation 1.3 runs over, and $A$ is the number of nucleons.

In practice, only a finite number of relevant states are considered in the calculations, such that the dimension of the matrices is finite and significantly reduced. The wavefunction is hence approximated as the linear combination of a finite set of states $\{|\Phi\rangle_j\}_{j=1}^{N}$:

$$|\Psi_k\rangle \approx \sum_{i=1}^{N} C_k^j |\Phi\rangle_j. \tag{1.6}$$

The subspace spanned by the truncated basis $\{|\Phi\rangle_j\}_{j=1}^N$ is normally referred to as the *model space* or *valence space*. The single particle levels *below* the valence space compose the *core* and are generally considered fully occupied.

Because of this truncation, the residual interaction in the shell-model Hamiltonian (see Equation 1.2) is not the bare nucleon-nucleon interaction. Instead, it is an effective interaction that must be tailored to the truncated basis. In principle, this effective interaction must be determined by ensuring that the observables calculated within the truncated model space coincide with those observed experimentally.

## 1.3 The N=20 island of inversion

Due to the major role played by the residual term in the interactions, the so-called intruder states arise when moving away from the valley of $\beta$ stability. These correspond to configurations where one or more nucleons deviate from the expected shell-filling pattern and occupy energy levels that would normally be higher in energy, according to standard shell model calculations. Intruder states can have a significant impact on the behavior and properties of a nucleus, including its shape, stability, and spectroscopic features.

In the region along the neutron-rich $N = 20$ shell closure, the ground-state structure of certain isotopes is known to be dominated by intruder configurations, where neutrons occupy states above the $N = 20$ shell gap while leaving vacancies in the shell below [6]–[8]. An example of such nuclei is $^{32}$Mg (see Figures 1.2 and 1.3), which presents a deformed ground state corresponding to the intruder configuration. Other neighboring nuclei present similar features, constituting the so-called “island of inversion”. This trend extends to nearby nuclei where, although the ground states follow the shell-model ordering, sets of intruder states have been found within their excited states. These sets are often referred to as intruder bands.

Conversely, the intruder band, observed along the $N = 20$ isotonic line in neighboring nuclei, remains unseen in $^{35}$P [9]. According to Monte Carlo shell-model calculations [10], [11], this band is expected to lie on a $1/2^+$ state at $\sim$3 MeV. The same calculations suggest that the already-observed $5/2^+_1$ state belongs to a 2 particle - 2 hole deformed intruder band, contrary to the interpretation provided by spectroscopic factor measurements [12].

Moreover, moving two protons from $^{32}$Mg along the $N = 20$ isotonic line, an abrupt change is observed in the structure of $^{34}$Si. This isotope presents enhanced stability with respect to the nuclei in the surrounding, while being the first even-even isotope outside the island of inversion [13]. States related to both the spherical and intruder configurations emerge at similar excitation energies and, hence, understanding the nature of these states and the interplay between the two configurations represents an interesting case of study.

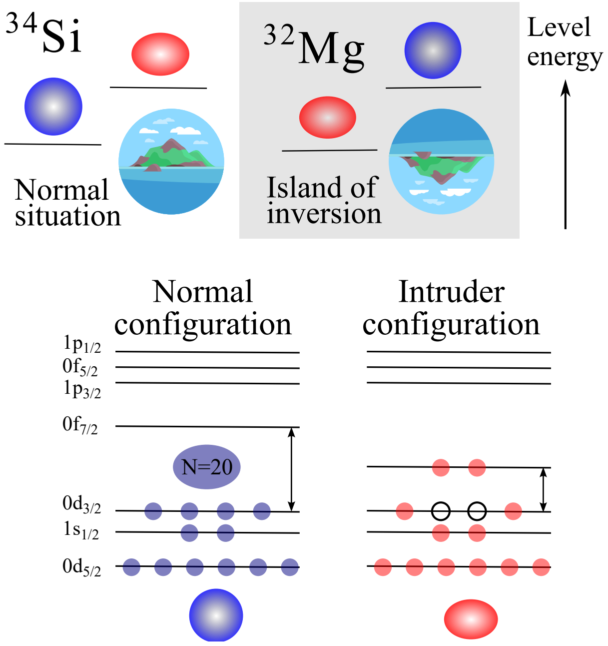

Figure 1.2: Visual representation showcasing the differences between *conventional* shell model configurations and intruder configurations. Intruder states typically involve nucleons breaking the normal shell model filling pattern, often occupying higher energy levels. They can lead to unique phenomena, such as nuclear deformation.

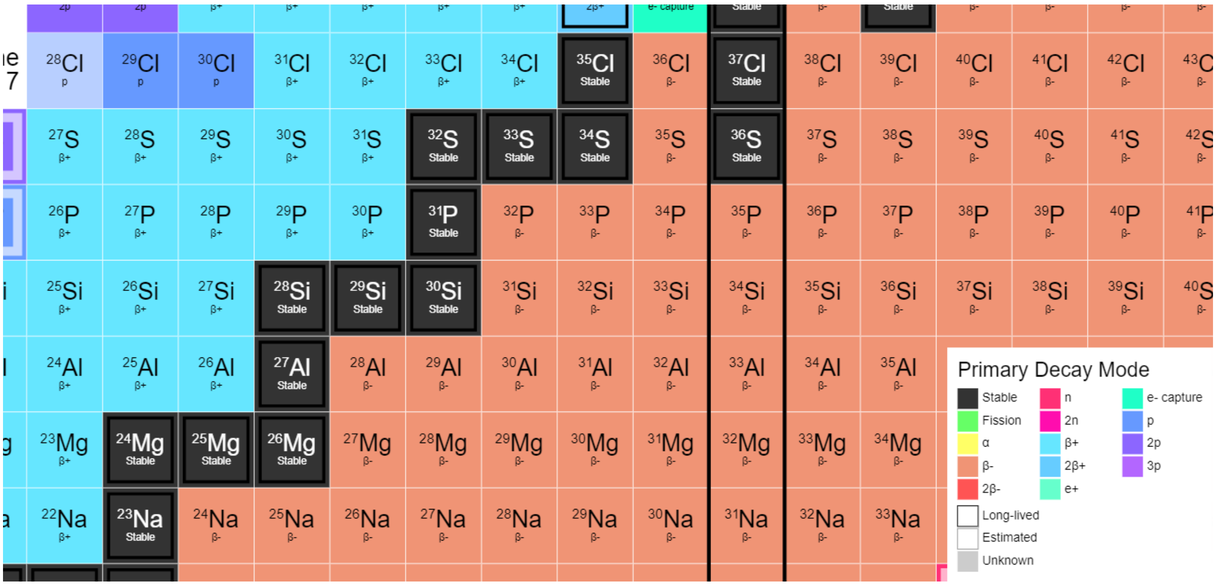

Figure 1.3: Nuclear chart focused on the neutron-rich region of the $N = 20$ isotonic line. The color scheme of the chart represents the main decay mode. Figure adapted from [14].

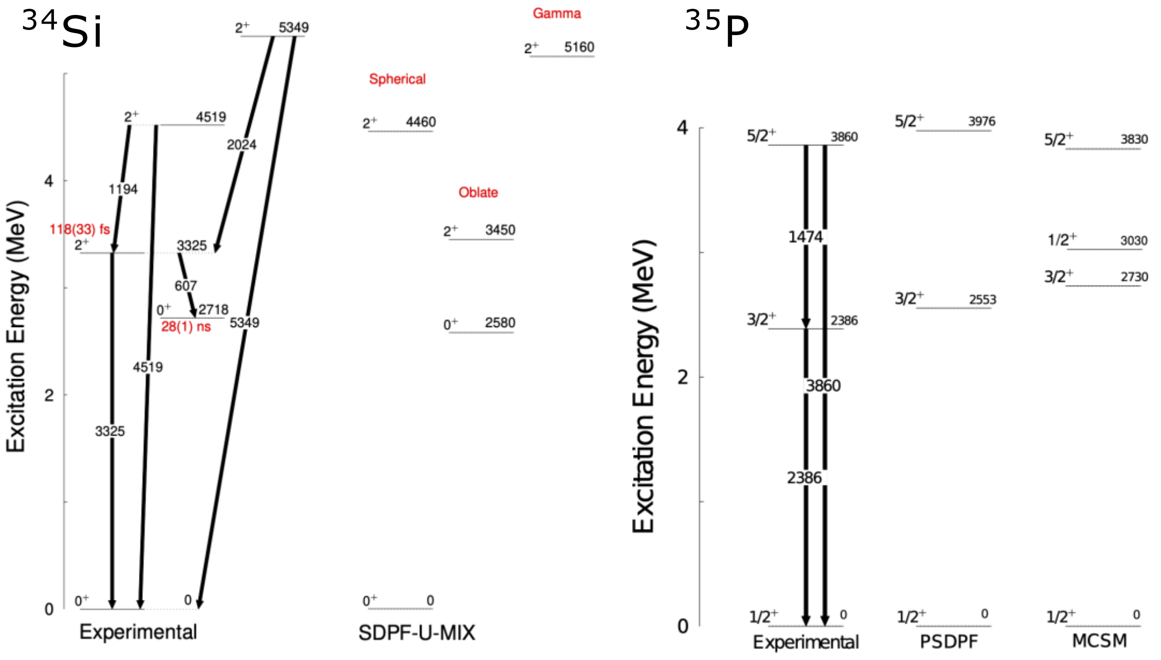

Figure 1.4: Experimental level schemes for $^{34}$Si (left) and $^{35}$P (right). On the right of each, the theoretical calculations and the predicted nature of each state are indicated.

In particular, Shell-Model (SM) calculations have been performed with the SDPF-U-MIX [15] interactions and compared to experimental measurements to investigate the nature of the excited states. While theory and experiments agree on the nature of the first $2^+$, assumed to correspond to an intruder configuration, opposite interpretations are presented for the second $2^+$: shell-model calculations predict a spherical nature of the $2^+_2$ state of $^{34}$Si, whereas the authors of Reference [16] attribute that state to the intruder band, based on the $\gamma$-branching ratios measured in the $\beta^-$ decays of $^{34}$Mg and $^{34}$Al.

### 1.3.1 Transition probabilities and nuclear lifetimes

A comparison of experimental measurements with theoretical models requires characterizing the wave-function of nuclear excited states. However, the wave-functions are not a physical observable and, experimentally, the information must be indirectly derived from some observable quantity $\langle i|\hat{\mathcal{O}}|f\rangle$, such as the mass, spin, parity, excitation energy, or transition probabilities between the nuclear excited states.

Transition probabilities offer a valuable tool for spectroscopic studies. By deducing the reduced transition probabilities from the corresponding electromagnetic operators, one can determine the overlap between the initial and final wave-functions.

The reduced transition probability is defined as

$$B\left(\sigma L; J_i \to J_f\right) = \frac{1}{2L+1}\left|\langle J_f||\mathcal{O}(\sigma L)||J_i\rangle\right|^2. \tag{1.7}$$

Here, $\sigma$ represents the transition character (electric $E$ or magnetic $M$), $\mathcal{O}(\sigma L)$ the electromagnetic operator and $L$ the multipolarity (see Section 1.3.2). This spectroscopic information can be calculated theoretically or obtained from experimental measurements of related quantities.

Reduced transition probabilities are frequently extracted from measured lifetimes. By comparing lifetime measurements with theoretical predictions, it becomes possible to validate and refine the theoretical models. Discrepancies between theory and experiments can lead to a deeper understanding of the underlying nuclear structure. The lifetimes of electromagnetic transitions are related to the reduced transition probabilities as [17]

$$\tau^{-1}(\sigma L; J_i \to J_f) = \frac{8\pi(L+1)}{\hbar L[(2L+1)!!]^2} \left(\frac{E_\gamma}{\hbar c}\right)^{2L+1} B\left(\sigma L; J_i \to J_f\right). \tag{1.8}$$

### 1.3.2 Selection rules of electromagnetic transitions

The $\gamma$ rays emitted in an electromagnetic decay carry angular momentum from the nuclear system. The angular momentum carried by the photon, $\vec{L}$, must fulfill the angular momentum conservation rule

$$\vec{J}_i = \vec{L} + \vec{J}_f, \tag{1.9}$$

where $\vec{J}_i$ and $\vec{J}_f$ are the angular momenta of the initial and final states, respectively. This implies that

$$|J_i - J_f| \leq L \leq J_i + J_f. \tag{1.10}$$

Moreover, $\gamma$ rays can be of an electric ($E$) or magnetic ($M$) character, which is related to the change in parity between the states. The selection rules are:

$$\pi(EL) = (-1)^L \tag{1.11}$$

$$\pi(ML) = (-1)^{L+1}. \tag{1.12}$$

An approximation to single-particle matrix elements is commonly used to define comparative units for the probability of emitting a photon of electric or magnetic character. These are given by the so-called *Weisskopf estimates* [17]:

$$\lambda(EL) = \frac{8\pi(L+1)}{L[(2L+1)!!]^2} \frac{e^2}{4\pi\epsilon_0 \hbar c} \left(\frac{E_\gamma}{\hbar c}\right)^{2L+1} \left(\frac{3}{L+3}\right)^2 cR^{2L}, \tag{1.13}$$

$$\lambda(ML) = \frac{8\pi(L+1)}{L[(2L+1)!!]^2} \left(\mu_p - \frac{1}{L+1}\right)^2 \left(\frac{\hbar}{m_p c}\right)^2 \frac{e^2}{4\pi\epsilon_0 \hbar c} \left(\frac{E_\gamma}{\hbar c}\right)^{2L+1} \left(\frac{3}{L+3}\right)^2 cR^{2L-2}, \tag{1.14}$$

with $m_p$ the proton mass, $\mu_p$ the proton magnetic moment, $E_\gamma$ the energy of the $\gamma$-ray emitted in the transition, $A$ the atomic mass and $R$ the nuclear radius ($\approx 1.2\ A^{1/3}$ fm).

The character of the transitions is dominated by the lowest allowed multipolarity $L$, provided that parity is conserved ($E$ or $M$ transitions). Notably, a transition from a $2^+$ state to a $0^+$ state can only be an electric transition of $L = 2$ ($E2$).

Table 1.1 provides the Weisskopf estimates for electric and magnetic transitions as a function of the multipolarity $L$ and the mass $A$. The values of each Weisskopf estimate as a function of the energy of the emitted photon for $A = 35$, i.e. the mass range of interest, are displayed in Figure 1.5.

Table 1.1: Values of Weisskopf estimates depending on the energy of the transition ($E$) and the atomic mass ($A$) for different values of L and for the electric and magnetic transition. From Reference [18].

| Electric multipole $[s^{-1}]$ | Magnetic multipole $[s^{-1}]$ |
|---|---|
| $\lambda(E1) = 1.0 \times 10^{14} A^{2/3} E^3$ | $\lambda(M1) = 5.6 \times 10^{13} E^3$ |
| $\lambda(E2) = 7.3 \times 10^{7} A^{4/3} E^5$ | $\lambda(M2) = 3.5 \times 10^{7} A^{2/3} E^5$ |
| $\lambda(E3) = 34 A^{6/3} E^7$ | $\lambda(M3) = 16 A^{4/3} E^7$ |
| $\lambda(E4) = 1.1 \times 10^{-5} A^{8/3} E^9$ | $\lambda(M4) = 4.5 \times 10^{-6} A^{6/3} E^9$ |

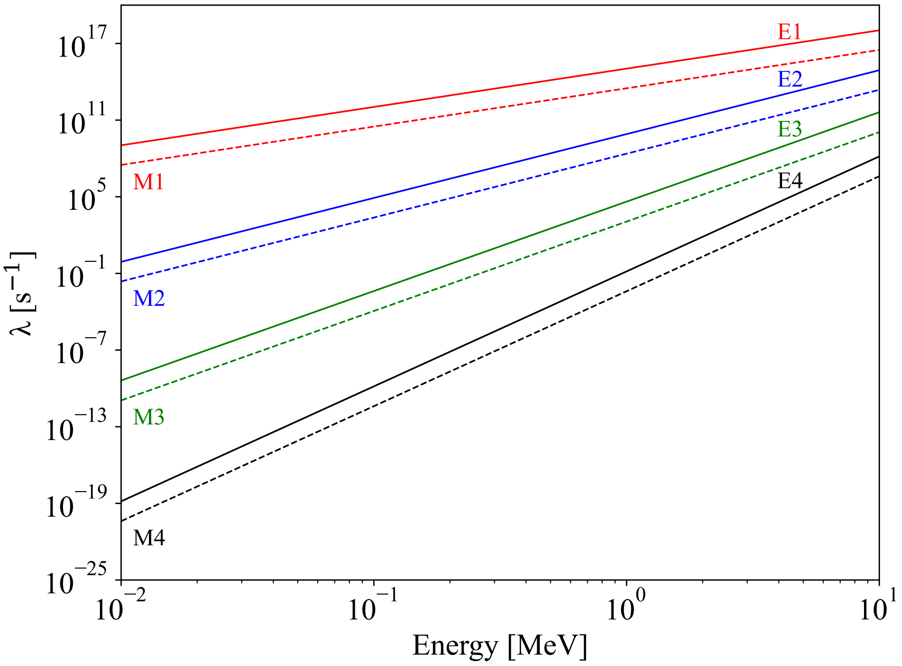

Figure 1.5: Weisskopf estimates for A=35.

## 1.4 Objectives of the thesis

The techniques employed to measure lifetimes, or absolute transition probabilities, must be tailored to obtain sensitivity to the decay products and to cover an enormous time scale spanning from $10^{-20}$ s to many years. In this work, the focus is driven towards lifetimes in the range of tens to hundreds of femtoseconds, which cannot be accessed through direct timing techniques. Yet, lifetimes of excited nuclear levels in this range can be indirectly measured by the Doppler-shift methods, namely the recoil distance plunger method (RDM) and the Doppler Shift Attenuation Method (DSAM), the latter being the approach employed in this analysis. For further details on the method, see Section 2.3.

An experiment aimed to study the interplay of spherical and intruder configurations in the low-lying states of isotopes on the edge of the island of inversion was performed at the Laboratori Nazionali di Legnaro (LNL) in November 2022. In particular, the experiment aimed to study the lifetime of the first two $2^+$ states of $^{34}$Si and the $5/2^+_1$ state of $^{35}$P using the Doppler Shift Attenuation Method. The focus of this work was to analyze the experimental data, from the calibration of the individual detectors to the measurement of the lifetime of the $2^+_1$ state in $^{36}$S via DSAM. The overarching aim was to establish the validity of the DSAM technique while also identifying and addressing any potential challenges that may arise during the analysis process. Furthermore, this work paves the way for the analysis of aforementioned states in $^{34}$Si.

# 2

# Experimental set-up and methodology

In this Chapter, the experimental setup and the detectors used will be described. The experiment was performed using the beam provided by the TANDEM-ALPI accelerator complex at the Legnaro National Laboratories (Legnaro, Italy) in November 2022, during 8 days of beam time. The low-lying states of the isotopes of interest were populated via a multinucleon transfer reaction using a beam of $^{36}$S at 230 MeV. The beam, with an intensity of 2 pnA, impinged on a 1 mg/cm$^2$ target of $^{208}$Pb, tilted of 45°, deposited on a 4 mg/cm$^2$ layer of Pd. The Pd backing is a necessary component to perform the lifetime measurement using the Doppler Shift Attenuation Method (DSAM), and its thickness was optimized to achieve a sensitivity in the range between $20 - 300$ fs.

The beam-like fragments were detected using the PRISMA magnetic spectrometer [19], placed at 51° with respect to the beam axis. This position was chosen to maximize the cross section to populate $^{34}$Si; the predicted angular distribution is shown in Figure 2.1. The recoiling ions reached PRISMA with an energy of $\sim$ 4.3 MeV/ u, sufficient for a good identification in mass ($A$) and atomic number ($Z$). Moreover, information on the velocity is used to implement an event-by-event Doppler correction of the $\gamma$-ray spectra. The $\gamma$ rays were detected using the Advanced GAmma Tracking Array (AGATA) [20], triggered by the PRISMA spectrometer.

## 2.1 The magnetic spectrometer PRISMA

Situated downstream of the scattering chamber, the high-acceptance PRISMA magnetic spectrometer [19] serves for the $Z$ and mass identification of reaction fragments. Its design allows for the identification of isotopes with masses ranging from $A = 20 - 150$, entering the spectrometer with energies between $E = 2 - 10$ MeV per nucleon.

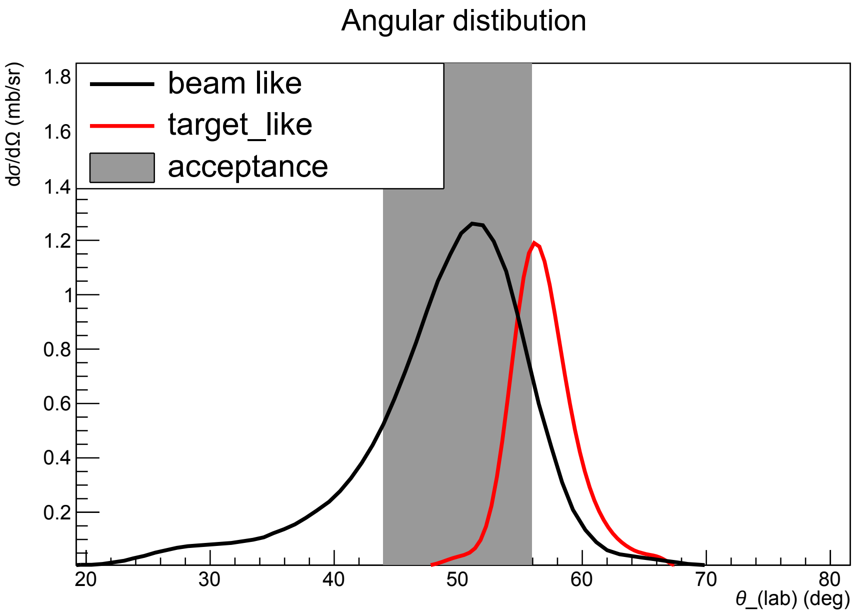

Figure 2.1: Experimental angular distribution for $^{34}$Si, as predicted by the `GRAZING` code. The maximum of the cross section corresponds to the grazing angle. The angular coverage of PRISMA appears highlighted in gray, the angle of PRISMA was set to maximize the beam-like particle influx.

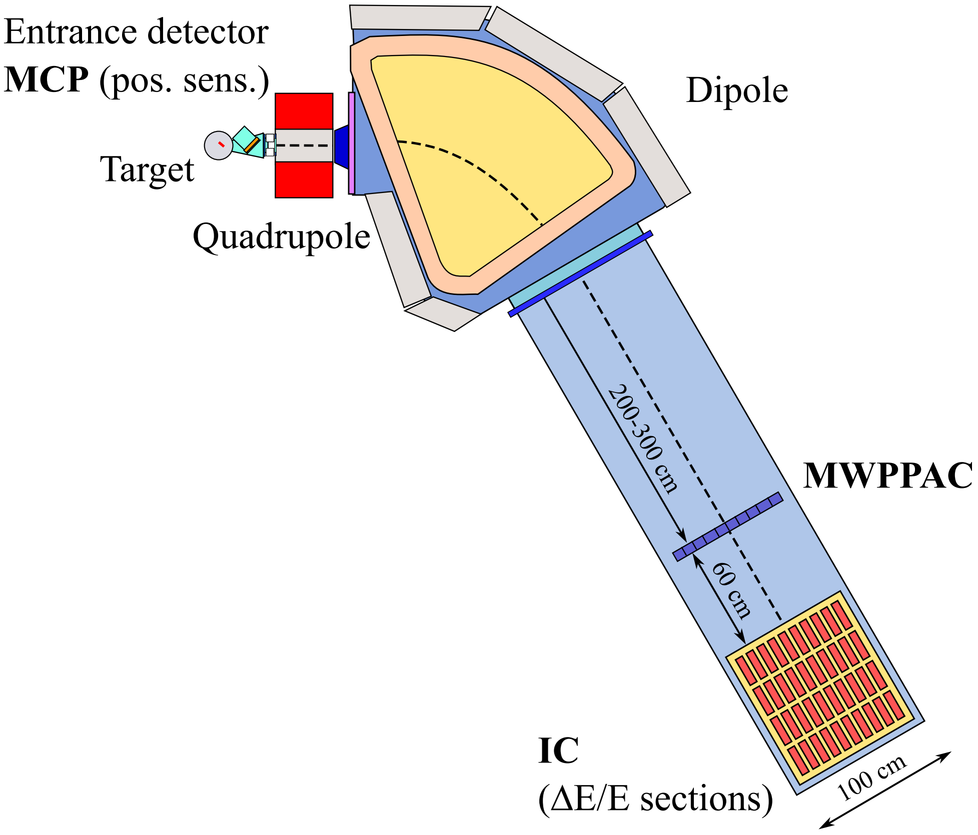

Figure 2.2: Schematic view of the PRISMA magntic spectrometer used for particle identification. Figure adapted from [19], [21].

PRISMA is composed of three detectors: the Micro-Channel-Plate (MCP) [22], a Multi-wire Parallel-Plate Avalanche Counter (MWPPAC) and an Ionization Chamber (IC) [23] and two optical elements: a quadrupole single and a dipole. A schematic representation of the PRISMA spectrometer is provided in Figure 2.2.

The operation principle of PRISMA is the following:

1. After the reaction, the particles are detected by the two-dimensional position and time-sensitive MCP detector [22], which serves as the entrance detector. Here, the $x_0$ and $y_0$ position of the particles are recorded, along with the first time signal, $t_0$, which is used to reconstruct the Time-of-Flight (ToF).
2. Next, the reaction fragments are focused in the vertical axis ($y$ axis) and defocused in the horizontal direction ($x$ axis) by the quadrupole single.
3. The particles then enter a dipole magnet, with a bending radius of 1.2 m [19]. Inside the dipole, the particle trajectories bend according to the magnetic rigidity ($B\rho$) of the ions, enabling the charge state and mass identification of the reaction fragments at a later stage in the analysis.
4. The ions then reach the MWPPAC detector [23], located in the focal plane of the spectrometer at a distance of approximately $\sim 200 - 300$ cm from the dipole. The MWPPAC detector records the second time signal, $t_1$, used for ToF reconstruction and the $(x_1, y_1)$ position in the focal plane.
5. Finally, the particles are stopped in the IC, where the energy loss and total energy of the fragments is measured so as to determine the $Z$ of the reaction fragments using the $\Delta E - E$ technique.

The spectrometer can rotate in a range from $-20°$ to $+130°$ with respect to the beam axis, and covers a solid angle of $\simeq 80$ msr (corresponding to a geometrical acceptance of $\pm 6°$ in the polar and $\pm 11°$ in the azimutal directions) [24]. The momentum acceptance of the spectrometer is $\pm 10\%$ and the dispersion is of $\simeq 4$ cm per percent in momentum. The mass and charge-state identification relies entirely on the software reconstruction of the particle trajectories. For this purpose, the event-by-event information on the entrance, $(x_0, y_0)$, and exit, $(x_1, y_1)$, positions is employed, as well as the ToF signal.

### 2.1.1 The Micro-Channel-Plate entrance detector

The entrance detector of PRISMA, located between the target and the quadrupole magnet of the spectrometer, consists of a pair of large-area rectangular ($80 \times 100$ mm$^2$) fast-timing MCP detectors, placed about $\simeq 250$ mm after the target in chevron configuration [22]. A schematic representation of the detector is provided in Figure 2.3b.

The detector operates on the basis on an electrostatic field, which accelerates secondary electrons emitted from a thin carbon foil ( $20\mu g/cm^2$) when charged particles pass through it. Each MCP is composed of a position-sensitive anode, made of a 100 $\mu$m gold-plated tungsten delay line, which allows to extract the $x$ and $y$ entrance position information of the reaction products. To establish some reference points for position calibration of the detector's output, a cross-shaped mask has been put in front of the MCP.

The detection efficiency is nearly 100% for heavy ions with $A \gtrsim 60$ , and the position resolution is of approximately 1 mm in both the $x$ and $y$ directions. The time resolution of the detector is of $\sim 400$ ps.

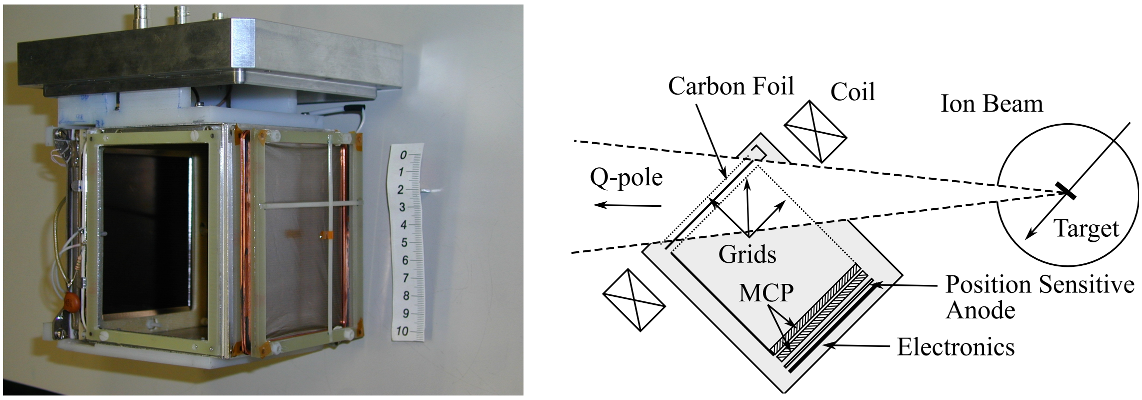

(a)

(b)

Figure 2.3: The MCP entrance detector of PRISMA (a) picture and (b) schematic representation of its components. Taken from reference [22].

## 2.1.2 The Multi-wire Parallel-Plate Avalanche Counters

The MWPPAC detector, located at the focal plane of PRISMA, enables the measurement of the $x$ and $y$ ion positions and timing [23]. The detector has a three electrode configuration comprising a central cathode and two wire planes for the $x$ and $y$ anodes, arranged orthogonal to each other. The wires, composed of gold-plated tungsten with a diameter of 20 $\mu$m, cover an area of $13 \times 100$ cm$^2$. The $x$ anode plane and cathode are divided into 10 equal and independent horizontal sections, each measuring 10 cm in length and equipped with vertical wires. The $y$ plane, on the other hand, utilizes horizontal wires. The wire spacing in the $x$ and $y$ planes is 1 mm, while the cathode spacing is 0.3 mm. The detector is equipped with mylar input and exit windows and is filled with isobutane gas ($C_4H_{10}$) at a pressure of $7-8$ mbar. The position resolution of the detector is of $\sim 1$ mm, while the time resolution is similar to that of the entrance detector, that is $300-400$ ps.

Moreover, the OR of the cathode sections serves as the trigger for the PRISMA acquisition. The time information of the MWPPAC and MCP is combined in order to measure the ToF. Figure 2.4 shows a sketch and a picture of the detector.

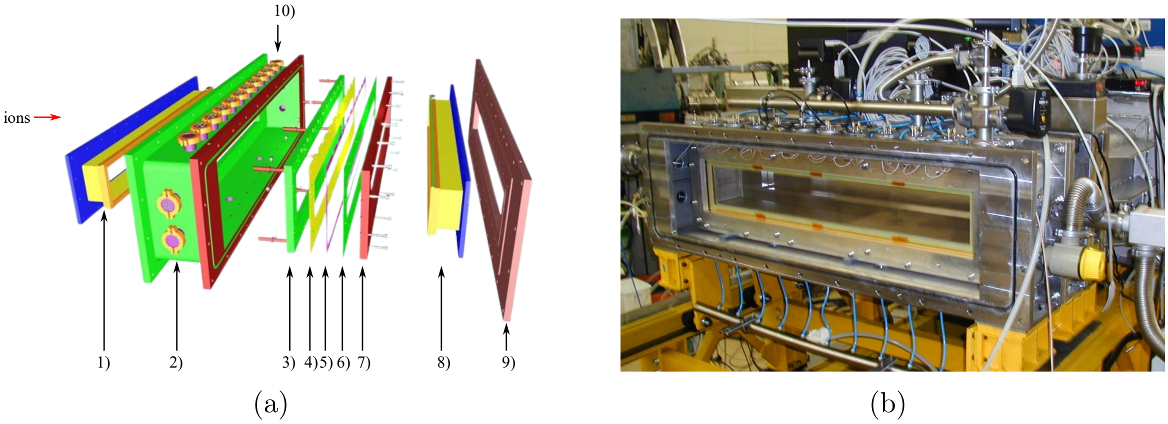

(a) (b)

Figure 2.4: The Multi-wire Parallel-Plate Avalanche Counters (MWPPAC) detector of PRISMA (a) exploded view and (b) front-view. In (a) its various components are identified: 1) Input window, 2) vacuum vessel, 3) aluminum X frame, 4) X printed-circuit board, 5) vetronite spacer, 6) cathode-Y printed-circuit board, 7) aluminum cathode-Y frame, 8) exit window, 9) matching connection flange, 10) individual electrical connections for each section. Figures taken from [23].

### 2.1.3 The Ionization Chamber (IC)

The PRISMA ionization chamber, located 60 cm downstream from the MWPPAC, consists of a $110 \times 20 \times 120$ cm$^3$ volume chamber filled with either carbon tetrafluoride ($CF_4$) or high-purity methane ($CH_4$). The spacious design allows for the use of low gas pressure, up to 100 mbar, to stop the ions. The ionization chamber features 40 electrodes in the form of pads: 10 horizontal sections similar to the MWPPAC and 4 sections in the $z$ direction (A, B, C, D), with each pad providing an independent $\Delta E$ measurement.

Additional side pads are situated at the ends of each row, which serve as veto detectors for trajectories exiting the chamber. The gas pressure is optimized for each experiment in order to ensure that most ions of interest stop between the C and D sections of the chamber. The total energy ($E$) of the ions is determined by summing the partial energy loss across all sections, while the $\Delta E$ measurement corresponds to the signal detected in the A or A+B sections.

The energy loss by the recoiling ions $-\langle dE/dx \rangle$, inside the IC is given by the Bethe equation:

$$-\left\langle \frac{dE}{dx} \right\rangle = \frac{4\pi e^4}{m_e} \cdot \frac{z^2}{v^2} \cdot n_e Z \cdot \left[ \ln\left( \frac{2 m_e v^2}{W} \right) - \ln\left(1 - \beta^2\right) - \beta^2 \right]. \tag{2.1}$$

Here, $z$ is the atomic number of the incident particle, $v$ its velocity and $\beta = v/c$, while $n_e$ and $Z$ are the electron density and atomic number of the medium, respectively. The quantity $W$ is the average energy needed to produce an electron-ion pair in the gas.

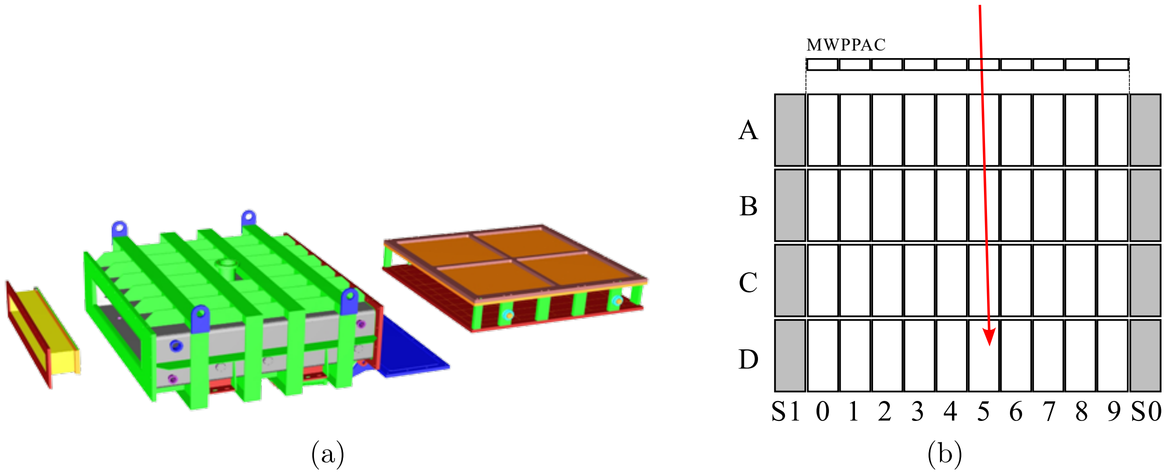

(a) (b)

Figure 2.5: Schematic layout of the components and pads of the PRISMA Ionization Chamber. (a) Taken from [23].

By plotting $\Delta E$ versus $E$, it becomes possible to identify different $Z$ values, with a resolution of approximately $1/60$. Figure 2.5 depicts a schematic drawing illustrating the configuration of the ionization chamber.

### 2.1.4 PRISMA optics and trajectory reconstruction

The magnetic elements of PRISMA consist of a quadrupole and a dipole magnet. The quadrupole is placed 500 mm downstream the target, and its function is to focus the incoming ions in the vertical axis, while defocusing them in the horizontal direction. Then, the dipole is used to bend the particle trajectories according to the magnetic rigidity of the ions, thus allowing for the $A/q$ identification of the reaction fragments.

The mass and charge identification of the ions relies on an event-by-event trajectory reconstruction, which uses the variables measured by the MCP, MWPPAC and IC detectors (calibrated entrance and focal plane positions, ToF and energy loss) and the equations of motion of charged particles in the presence of magnetic elements. The software reconstructs the ion trajectories based uniquely on two parameters: the ratio between the quadrupole and dipole magnetic fields and the curvature radius in the dipole. The algorithm first determines the curvature radius based on the entrance and focal plane positions. Then, the tracking algorithm searches for the parameters that match best the experimental data. The output are the radius inside the dipole magnet ($\rho$), the path length, the total energy (via ToF) and the mean path of the ions in the IC.

## 2.2 The AGATA $\gamma-$ray tracking spectrometer

AGATA (Advanced GAmma Tracking Array) [20], [25] is a new-generation $\gamma$-ray tracking High-Purity Germanium (HPGe) detector array. It is currently in operation at the Laboratori Nazionali di Legnaro (LNL) facility and it is used for high-precision $\gamma$-ray spectroscopy. The AGATA project aims at the development of a full $4\pi$ $\gamma$-ray tracking array, similar to its counterpart GRETA [26], operative in the United States.

The high precision of AGATA is achieved by means of high-purity germanium, as well as the utilization of Pulse Shape Analysis (PSA) and tracking algorithms. PSA techniques are used to locate the interaction points of the $\gamma$ rays within the germanium array, which is made possible through crystal segmentation and fast digital acquisition electronics. Tracking algorithms enable the reconstruction of the full interaction path of the Compton-scattered $\gamma$ rays, based on the interaction points identified by the PSA. The use of these techniques and instrumentation results in a high photo-peak efficiency and peak-to-total ratio.

Presently, the detector has a $\sim 2\pi$ geometrical acceptance [25]. The angular resolution at nominal position is of $1^\circ$ [27], which leads to a reduction of the Doppler broadening and, thus, to an improved resolution for in-flight spectroscopy. For in-source measurements at 1 MeV, the energy resolution is of approximately 2‰ [20].

### 2.2.1 The AGATA detectors

The AGATA detectors consist on encapsulated and electrically segmented HPGe crystals. Each individual crystal is segmented into 36 sections, with a 6-fold segmentation along both the longitudinal and radial directions (see Figure 2.6a). These crystals are then assembled into 14 modular detectors, known as AGATA Triple Clusters (ATCs), where each ATC comprises three HPGe crystals placed within a tapered capsule. The crystals in the ATCs have an slightly asymmetric design, which are labelled as A - Red, B - Green and C - Blue (see Figure 2.6b).

The germanium crystals must be cooled to a temperature of 80 K. This is accomplished by placing the triple cluster in a cryostat which is periodically filled with liquid nitrogen. The AGATA Triple Cluster detector, along with its cryostat, is depicted in Figure 2.7a. The clusters are then mounted on a honeycomb structure, leaving a 0.5 mm spacing between neighboring clusters. The arrangement ensures a uniform coverage of the solid angle, with the smaller sides of the clusters facing towards the center of the reaction chamber. A picture of the array, together with the number labelling of the ATC corresponding to the present configureation of AGATA at LNL is illustrated in Figure 2.7b.

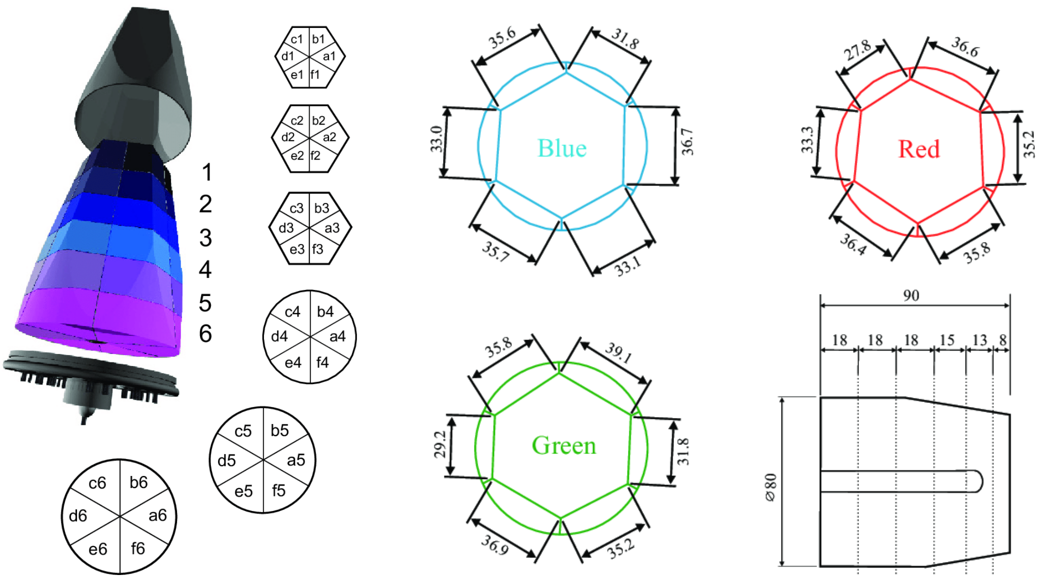

(a) (b)

Figure 2.6: (a) Segment labelling of the AGATA HPGe crystal. Each crystal is divided into six rings, which are labeled from 1 to 6. Each ring is further subdivided into six sectors in the radial direction, denoted by the letters a to f. (b) Illustration of the three distinct geometries of the AGATA crystals (A, B, C). The side view depicted in the lower right portion indicates the placement of the segmentation lines. All measurements are provided in millimeters. Both figures taken from [20].

### 2.2.2 Readout electronics

Each crystal has a total of 38 output channels: 36 channels are derived from the segments located on the outer surface of the crystal, while 2 channels come from the common core contact at the center with 2 different gains. The common core contact collects the signal from the negative charge carriers (electrons) generated during the interaction, while the contacts of the segments collect the signal from the corresponding positive charges (holes). Consequently, the signal amplitude measured by the common core contact is equivalent to the sum of the signals in the segments for each interaction. The detector signals undergo initial processing by the AGATA Front-End Electronics (FEE), which consist of a set of specially designed charge preamplifiers and digitizers. These devices are designed to meet the requirements for precise timing properties and high counting rate capability (more than 50 kHz per crystal) [28].

To ensure high-quality and fast signals for PSA, the output signals from each crystal pass through specialized charge-sensitive preamplifiers installed on the ATCs. The signals are after transmitted via MDR cables to the digitizer modules. The digitizers, which have a sampling rate of 100 MHz and a resolution of 14 bits, are designed with a dedicated water cooling system to prevent overheating. Each digitizer unit consists of three modules, meaning that one unit serves one ATC, accommodating all three crystals.

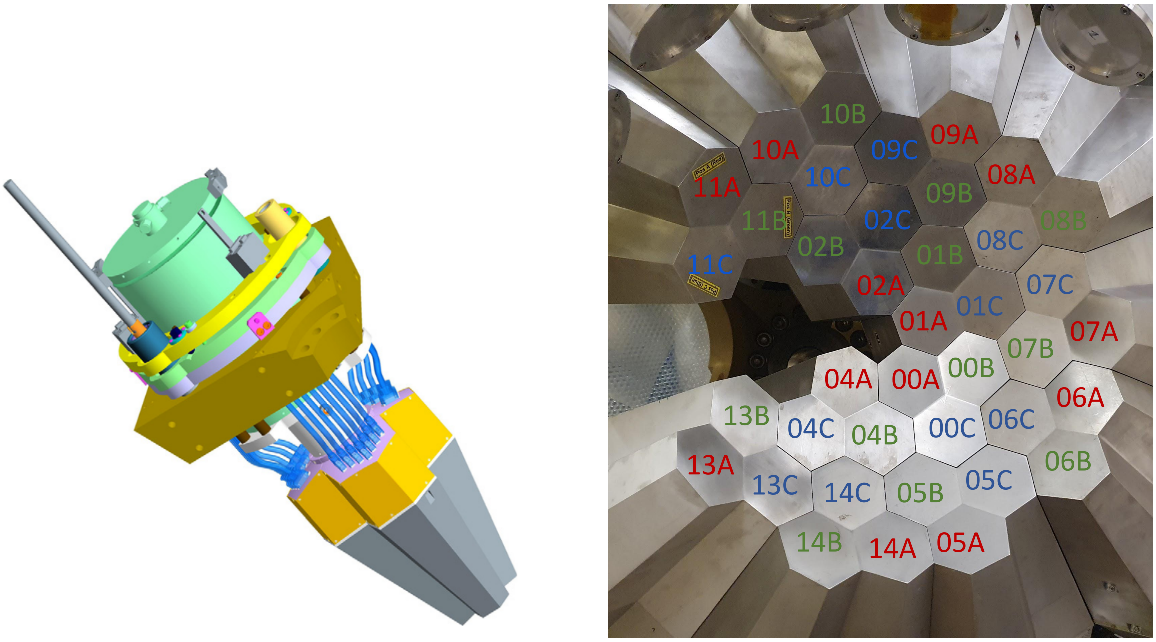

(a) (b)

Figure 2.7: (a) 3D rendering of an Agata Triple Cluster detector, along with its cryostat. Taken from [20] (b) The AGATA detector array at LNL with the position numbers for the ATCs.

The digitized signals are pre-processed using Field Programmable Gate Arrays (FPGAs), and a trapezoidal filter to extract the trigger time and energy information. The core signal functions as the trigger for the crystal. Upon the generation of a local trigger, a request is dispatched to the Global Trigger and Synchronization system (GTS). The GTS can be connected to a Trigger Processor (TP) to select events based on specific experimental requirements, such as particle-$\gamma$ coincidence events with PRISMA.

The output from the digitizers is then converted into optical signals and transmitted through fiber connections to the Global Gigabit Processor (GGP) boards located on the acquisition machines. These GGP boards are designed to handle a data rate of 2 Gbps per channel effectively.

### 2.2.3 Pulse Shape analysis (PSA)

The Pulse-Shape Analysis (PSA) is used for accurately identifying the positions of individual interaction points and the corresponding energy depositions of a $\gamma$ ray within the detector array. Typically, a $\gamma$ ray will undergo multiple interactions within the germanium shell (e.g. 3 to 4 interactions at 1.3 MeV). These interactions can occur within a single detector segment or involve scattering to another segment within the same crystal, an adjacent detector, or even across the shell. In order to perform the tracking process with high efficiency, high precission ($\sim$mm) in the identification of the interaction points is required.

The PSA compares the traces of the measured signal in each crystal segment with a library of segment-by-segment traces corresponding to a collection of simulated interactions, comprising a huge amount of calculated position-dependent detector pulse shapes in a grid of points that maps the whole crystal volume. This data base is called AGATA detector library (ADL) or also basis [29]. The position, deposited energy and time of the interaction is assigned according to the simulated pulses that fit best the measured signal.

When energy is deposited in a segment, opposite sign integrated charge signals are collected at the two electrodes of the segment. In the neighboring segments, transient signals are induced, resulting in a total collected charge of zero. Figure 2.8 provides an example of the net charge signal shape and the transient signals in the neighboring segments relative to the interaction. By analyzing both the net charge and transient signals, the PSA achieves a positional resolution better than the segment size, with a precision of a few millimeters [20].

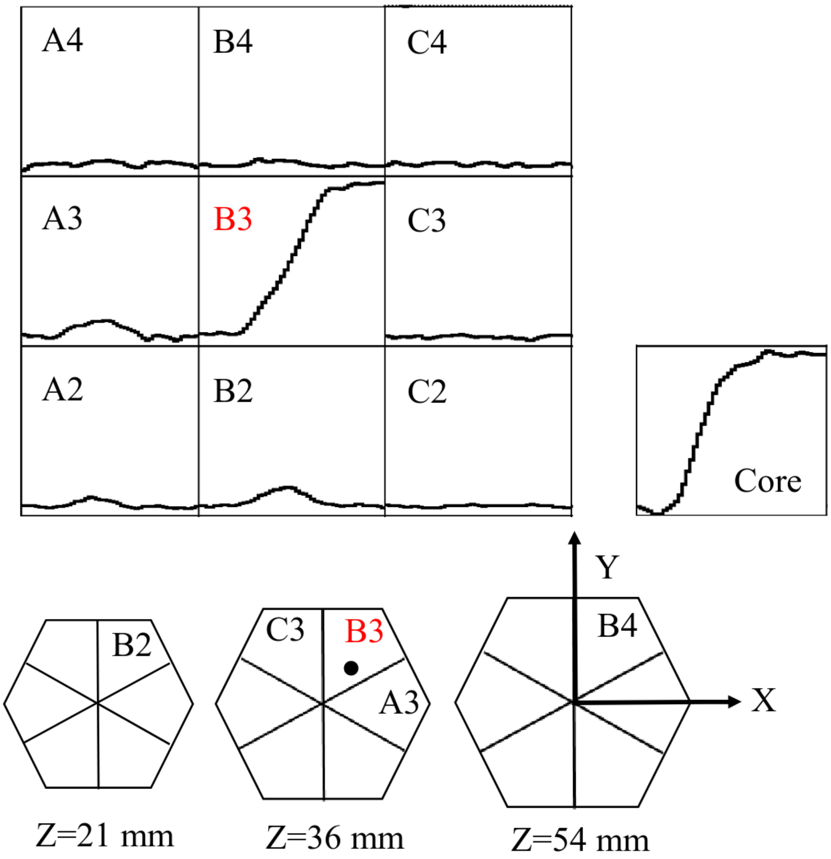

Figure 2.8: Net charges and transient signals for one event in an AGATA detector. The net charges are registered in the core and segment B3, where the interaction took place (indicated by a black dot). The induced mirror charges are seen in the neighbouring segments and indicate the position of the interaction inside the segment. Taken from [28].

### 2.2.4 Tracking algorithm

The interaction of photons with the medium occurs through various processes: primarily, in the energy regime of interest for high-resolution $\gamma$-ray spectroscopy, photoelectric absorption, Compton scattering, and pair production [30]. The dominant effect is determined by the energy of the incident photons (refer to Figure 2.9). The photoelectric effect is the primary interaction mechanism for photon energies below 150 keV. In this process, the entire energy of the incident photon is deposited in a single isolated interaction point. In the energy range of 100 keV to 10 MeV, Compton scattering becomes dominant. It involves a sequential scattering process of the photon, with the remaining energy being finally deposited through photoelectric effect. Above 1.022 MeV, pair production becomes possible. In this mechanism, the initial interaction point releases the total energy of the gamma-ray, excluding the mass necessary for creating an electron-positron pair. The resulting two photons from the annihilation process (511 keV) Compton scatter, generating their own sequences of interaction points in close proximity to the initial interaction point.

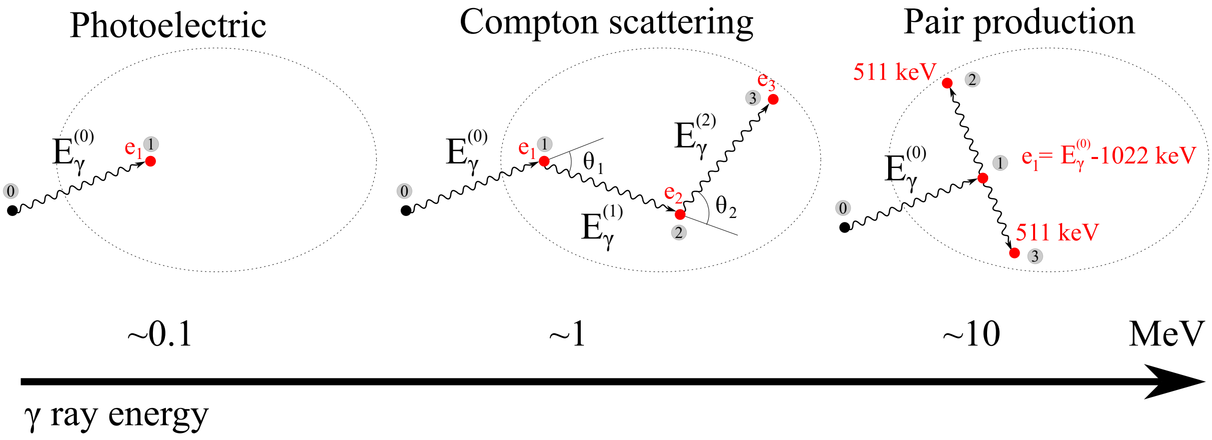

Figure 2.9: The most likely $\gamma$-ray interaction processes for different ranges of the $\gamma$-ray energy. Adapted from [28].

In the energy range typically encountered in spectroscopic analysis using AGATA (approximately 100 keV to 10 MeV), Compton scattering is the prevailing interaction process. As a result, a significant portion of the single interactions within the detector does not provide information about the total energy of the $\gamma$ ray.

The tracking algorithm uses the information on the individual interactions within the detector volume derived from the PSA to reconstruct the trajectory of the photon within the germanium crystal. This reconstruction enables the algorithm to combine the partial energy depositions, resulting in the precise determination of the full energy of the incident photon. As a result, the absolute photopeak efficiency is enhanced, and the peak-to-total ratio is improved. A detailed discussion on the tracking algorithms used for AGATA data processing can be found in Reference [31].

## 2.3 The Doppler Shift Attenuation Method (DSAM)

The DSAM is a technique designed to measure the lifetimes of short-lived nuclear states, typically falling within the range of approximately $10^{-11} - 10^{-14}$ s. This method involves analyzing the Doppler-Shift of $\gamma$ rays emitted by recoiling ions as they gradually decelerate in a degrader positioned immediately after the reaction target [17].

The energy of the $\gamma$-radiation emitted by an excited heavy-ion recoiling with velocity $v(t)$ is given by

$$E_\gamma(\theta, t) = E_\gamma^0 \left[ \frac{\sqrt{1-\beta^2(t)}}{1-\beta(t)\cos\theta} \right], \tag{2.2}$$

where $\beta(t) \equiv v(t)/c$ is the ratio of the ion velocity to the speed of light, $E_\gamma^0$ is the $\gamma$-ray energy emitted by the nucleus at rest and $\theta$ is the angle of observation of the $\gamma$-ray relative to the direction of the ion recoil. For $\beta(t) \ll 1$, one can neglect second and higher order terms and reduce the expression to

$$E_\gamma(\theta, t) = E_\gamma^0 \left[1 + \beta(t)\cos\theta\right] + \mathcal{O}(\beta^2). \tag{2.3}$$

As the ions decelerate in the degrader, the Doppler corrected spectra exhibit a continuous energy distribution between $E_\gamma^0$ and $E_\gamma(t_c)$, where $t_c$ is the time the ions need to stop in the degrader ($v_f \equiv v(t_c) = 0$) or, in the case of differential DSAM ($v_f > 0$), to pass through the degrader. This distribution corresponds to the radiation emitted by ions traveling with velocities ranging from the initial velocity $v_i$ to $v_f$.

For this kind of measurement, it is necessary to know the variation of the ion velocities with time as they pass through the degrader, i.e. the velocity function. It is derived from the *stopping power* equation, which describes the kinetic energy loss of charged particles as they traverse a medium. The stopping power can be separated in two contributions: nuclear and electronic.

At high velocities (where $\beta > 2\%$), the nuclear term can be neglected and the the electronic stopping power becomes the main contribution. The description of this regime is comparatively simpler, and various parametrizations have been developed to characterize the electronic stopping power [30].

Conversely, at low velocities, the nuclear term is dominant, resulting in significant deflections caused by Coulomb scattering between recoiling ions and the ions present in the stopping material [32]. Due to the scarcity of experimental data within this velocity range, theoretical approaches like the Lindhard, Scharff, and Schiøtt theory [33] are commonly used to describe the slowing down process at low velocities.

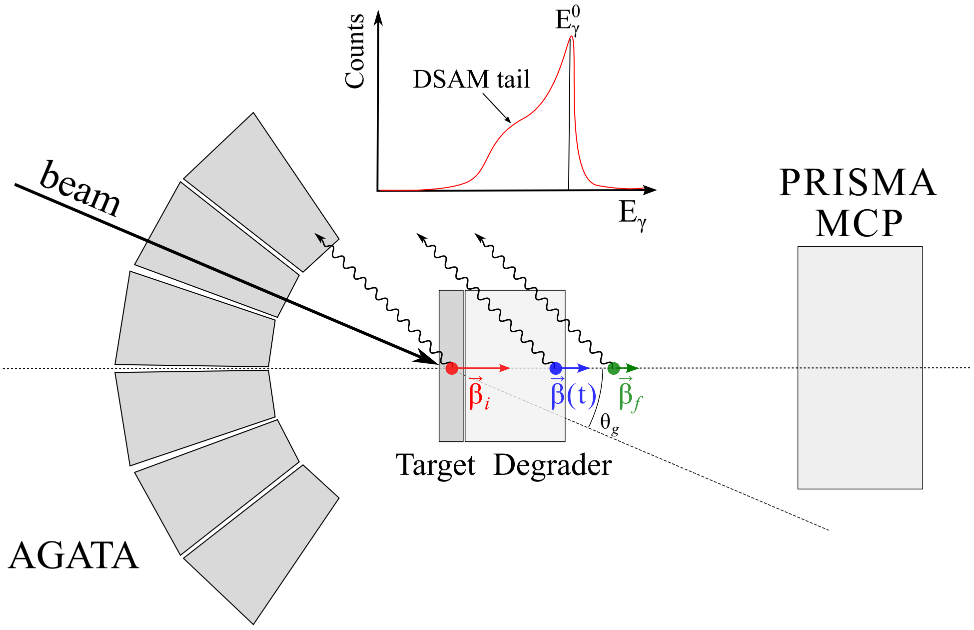

Figure 2.10: Diagram of the experimental setup: after passing through the target, the recoiling ions progressively slow down in the Pd degrader. The AGATA array is positioned outside the reaction chamber, covering the backward angles with respect to the beam direction. PRISMA spectrometer detects beam-like recoils at forward angles. Figure not in scale.

The derivation of the velocity function relies on different approaches tailored to the specific velocity range of the recoiling ions. Additionally, it is important to consider other factors in the experimental analysis, such as the scattering of recoiling ions in the degrader, the finite resolution of the detectors, the angular distributions of the recoils, and the initial velocity distribution. To incorporate all these to the analysis and obtain more accurate results, the lineshape analysis often relies on the use of Monte Carlo methods.

### 2.3.1 Line-Shape analysis and Monte Carlo methods

In the cases where the Doppler-shift broadening is greater than the detector resolution, nuclear lifetimes can be determined by analyzing the lineshapes of the Doppler-broadened peaks. This analysis involves comparing the experimental lineshapes with simulated lineshapes generated using Monte Carlo simulations for some set of lifetime values. The lifetime is extracted by means of a $\chi^2$ comparison with the experimental line-shape. In the present work, the Monte Carlo simulations are performed using the `GEANT4` software.

`GEANT4` is a widely used software toolkit for simulating the interaction of radiation with matter. In the simulations, the different interaction processes are treated as random events. To determine the specific interaction that occurs at each step, as well as other properties such as interaction positions or the $\gamma$-ray emissions, random samplers based on the physical Probability Distribution Functions are used.

# 3

# Data processing

In this Chapter the PRISMA+AGATA data processing will be discussed in detail. The PRISMA spectrometer allows for the identification of the beam-like reaction fragments on an event-by-event basis, as well as the observation of the $\gamma-$ray spectrum acquired in coincidence with the AGATA array.

Initially, the data processing of each detector is done separately. The various detectors of PRISMA are calibrated in order to obtain the mass spectrum with the highest $Z$ and $A$ resolution possible, as well as the velocity vector of the reaction products. The AGATA data undergoes two primary steps of processing. Firstly, during the *local level processing* phase, each crystal is handled individually. Subsequently, in the *global level processing*, data from the entire array is utilized to reconstruct the *tracked* $\gamma$-ray spectrum. Finally, the data from both detectors is merged in order to reconstruct the $\gamma$ spectra in coincidence with the recoiling ion species of interest, along with the necessary optimization procedures.

## 3.1 PRISMA data analysis

The aim of PRISMA is to provide an event-by-event identification of $Z$, $A$ and $\vec{\beta}$, to filter $\gamma$-ray events in coincidence with Advanced GAmma Tracking Array (AGATA). The data processing involves three main steps: first, the threshold and initial calibrations are set for all the raw electronic signals: Micro-Channel-Plate (MCP), Time-of-Flight (ToF), Multi-wire Parallel-Plate Avalanche Counter (MWPPAC) sections, and Ionization Chamber (IC) Pads. Then, the 2D $Z$ gates are set based on the $\Delta E$ versus $E$ matrix obtained from the IC signals. The trajectory reconstruction allows for a determination of the $A/q$, and the charge states $q$ can be selected for each $Z$ species combining the information given by the trajectory reconstruction and the IC. In the next sections, the PRISMA data processing will be discussed in detail.

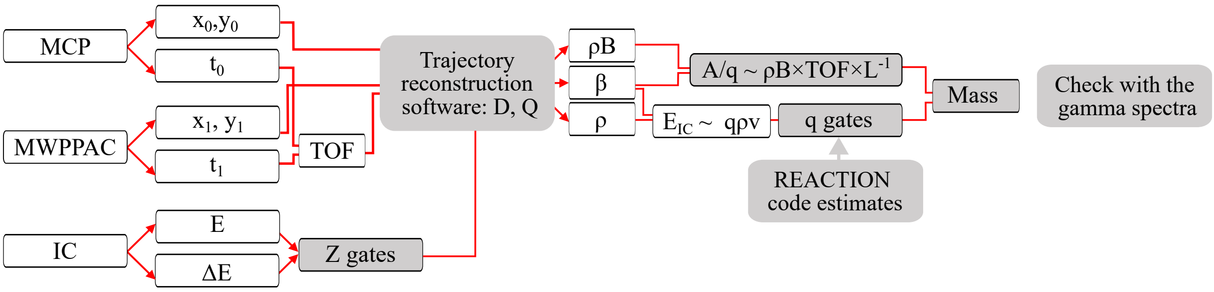

Figure 3.1: Strcuture of the PRISMA data processing.

## 3.1.1 Calibration of the MCP and the focal plane detectors

In this section the calibration of the MCP entrance detector and the focal plane MWPPAC and IC will be discussed.

### MCP calibration

The MCP entrance detector is designed to record the time and position of recoils as they enter the spectrometer, used for the reconstruction of the trajectory and velocity vector of incoming ions on an event-by-event basis.

At the data-processing stage, spurious events caused by inefficiencies and noise in the raw data are removed by setting a 2D gate, as shown in Figure 3.2. A metal cross is placed in front of the detector, creating a shadow in both spectra by partially blocking some incoming ions. The center of the cross and the marks on each arm (emphasized in Figure 3.2b) are used as reference points for calibrating the raw signals. The electronic signals are calibrated through a multi-parametric transformation, which allows one to account for possible deformations due to cross-talk effects between the $x$ and $y$ signals. The procedure is summarized herein.

First, a linear transformation is applied:

$$\begin{pmatrix} x' \\ y' \end{pmatrix} = \begin{pmatrix} 1 & x_1 \\ y_0 & 1 \end{pmatrix} \begin{pmatrix} x_{\text{raw}} \\ y_{\text{raw}} \end{pmatrix}. \tag{3.1}$$

Next, quadratic and linear calibrations are applied to the $x'$ and $y'$ coordinates respectively:

$$\begin{cases} x'' = a + bx' + c\,(x')^2 \\ y'' = d + ey' \end{cases}. \tag{3.2}$$

Finally, a $\theta$ angle rotation is implemented:

$$\begin{pmatrix} x_f \\ y_f \end{pmatrix} = \begin{pmatrix} \cos\theta & \sin\theta \\ -\sin\theta & \cos\theta \end{pmatrix} \begin{pmatrix} x'' \\ y'' \end{pmatrix}. \tag{3.3}$$

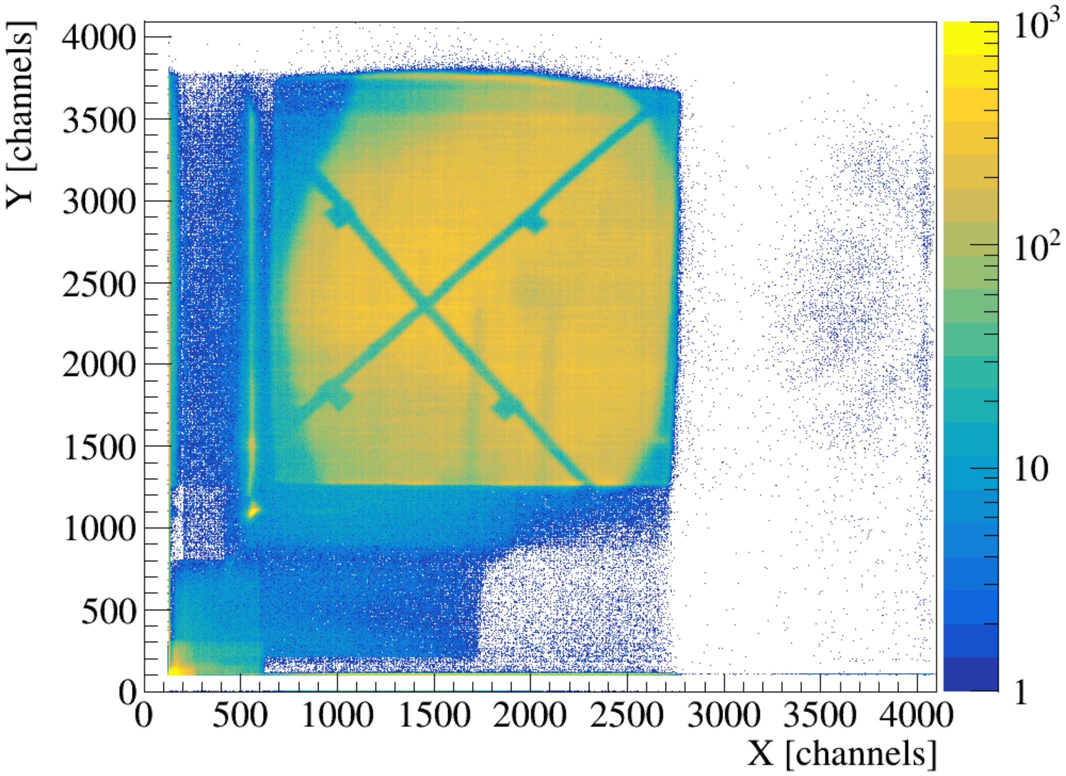

(a) Raw.

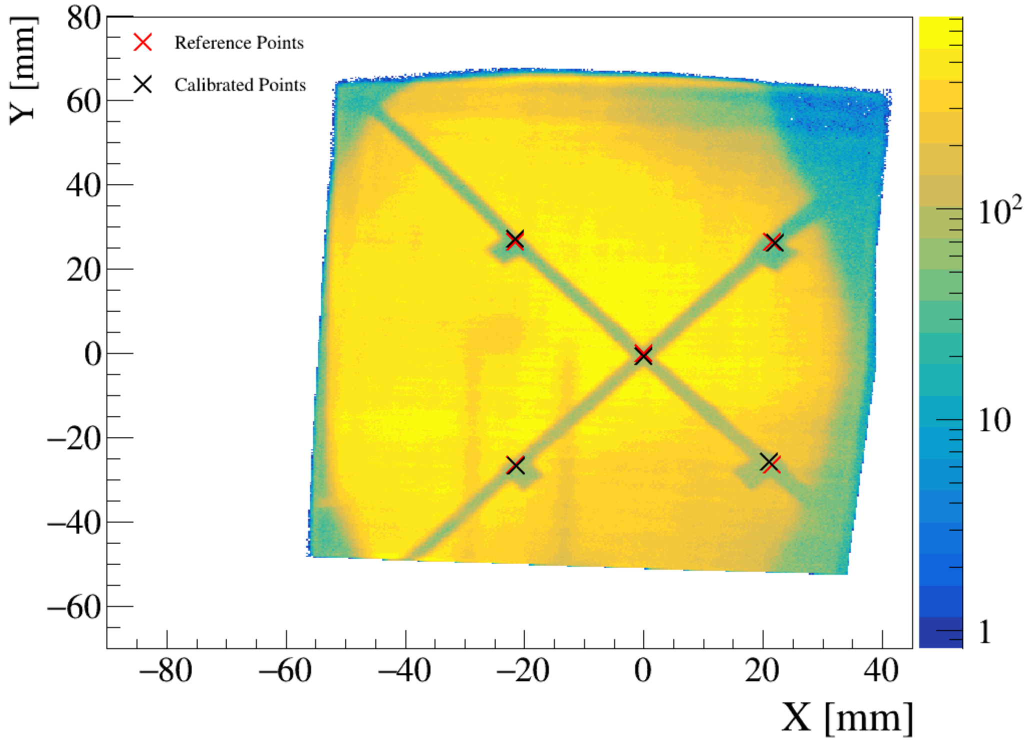

(b) Calibrated.

Figure 3.2: Comparison between the (a) raw and (b) calibrated MCP spectra. A 2D gate is used to remove the spurious events surrounding the detector. The reference points used as a reference for the calibration are indicated with a red cross in (b). The shadow seen at the center corresponds to two screws at the entrance of the quadrupole magnet.

Table 3.1: Positions of the reference points corresponding to the center and the flags on each arm of the cross placed in front of the MCP detector.

| Position | x [mm] | y[mm] |
|---|---|---|
| center | 0 | 0 |
| top left | -21.5 | 26.5 |
| top right | 21.5 | 26.5 |
| bottom left | -21.5 | -26.5 |
| bottom right | 21.5 | -26.5 |

The values of the parameters were obtained by minimizing the sum of the squared distances between the reference points real positions ($x_{\text{ref}}$ , $y_{\text{ref}}$ ), reported in Table 3.1, and their calibrated counterpart.

$$S = \sum_{i=1}^{N} \left[ (x_f - x_{ref})^2 + (y_f - y_{ref})^2 \right] \tag{3.4}$$

### MWPPAC calibration

The primary purpose of the MWPPAC detector, as described in Section 2.1.2, is to record the time and position of reaction products that reach the focal plane of the spectrometer. Additionally, the logical OR of all cathode signals is typically used as a trigger for the PRISMA read-out and data-acquisition system.

The detector provides a total of 32 electronic variables: the $x_{\text{left}}$, $x_{\text{right}}$ and *cath* (cathode) for each of the 10 horizontal sections of the MWPPAC and a common $y_{\text{up}}$ and $y_{\text{down}}$. When reconstructing the trajectories, it is assumed that they are planar, thus, calibrating the $x_{\text{left}}$, $x_{\text{right}}$, and *cath* variables is sufficient to determine the focal plane horizontal position, denoted as $x_{\text{fp}}$.

To retrieve the focal plane's horizontal position, a reference is taken from the edges and the center of each horizontal section, which exhibits a peak in the raw spectra due to the intentional shortening of the two central wires of each section's anode. In general, the focal plane position for each section is calculated as:

$$x_{\text{fp}}\,[\text{mm}] = a\,(x_{\text{right}} - x_{\text{left}}) + b, \tag{3.5}$$

where $a$ and $b$ are coefficients obtained through a linear fit of each section's center, right edge, and left edge. However, if one of the $x_{\text{left}}$ or $x_{\text{right}}$ signals is not recorded, the position can be still reconstructed by taking only one of $x_{\text{right}} - cath$ or $cath - x_{\text{left}}$.

#### Ionization Chamber calibration

The calibration of the IC detector, described in section 2.1.3 is done in two separate steps. The first step consists of the gain matching of all IC pads. This is performed during a separate calibration run (before or after the experiment) using a charge injector to deliver a known amount of charge directly to each individual IC pad. The second step involves setting upper and lower thresholds for the 48 segments. This is crucial for the 8 side pads, which serve as veto detectors. Any event producing a signal within the side pads' threshold is excluded from the analysis. Moreover, it was observed that pad C0 did not give any signal, as a consequence, column 0 had to be neglected in the analysis due to the inability to fully reconstruct the ion energy deposition.

#### Time of Flight calibration

The Time of Flight of the recoiling ions is determined by measuring the timing signals from the MCP entrance detector and the MWPPAC focal-plane detector. Each cathode section of the MWPPAC generates a timing signal for the start of the ToF signal, while the delayed signal from the MCP serves as the stop. Conversion from channels to ns is achieved via a linear calibration established in previous campaigns. However, the ToF signals of the various MWPPAC sections have to be aligned with each other by setting an individual offset for each section. Once all sections are aligned, a common offset is defined to determine the ion's correct ToF. The offset value is initially estimated based on the length of the ions' trajectory (approximately 6 meters) and the expected velocity of elastically scattered $^{36}$S nuclei, accounting for kinetic energy lost in the target. The initial estimation is then validated by examining the Doppler-shift correction of the energy of the $\gamma$ rays emitted by the recoiling ions in the AGATA spectra.

### 3.1.2 Z identification

After the data pre-sorting and the initial calibration of the detectors, polygonal $Z$ gates are set on the $\Delta E$ versus $E$ matrix, as $\Delta E \propto Z^2 \cdot \ln E$. Figure 3.3 displays the resulting $\Delta E - E$ spectrum obtained from the data collected by the PRISMA IC, along with the polygonal gates used to select different ion species and their corresponding identification. The beam itself, S, is the most intense channel.

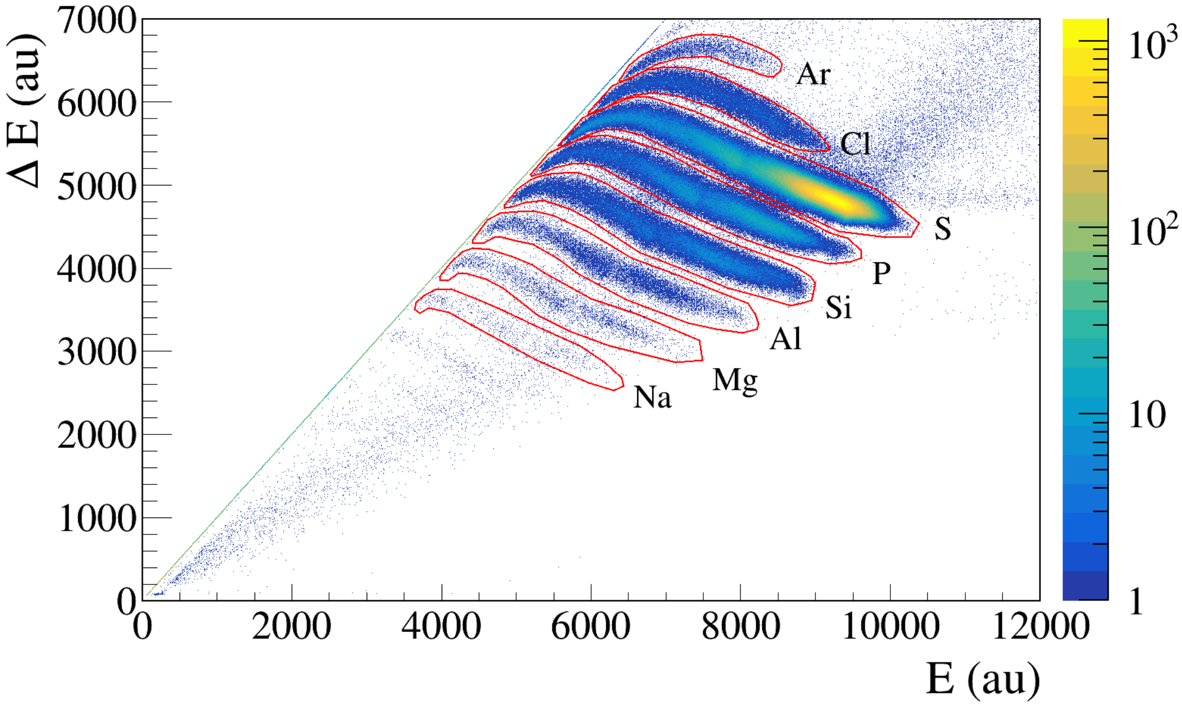

Figure 3.3: Experimental partial energy ($\Delta E$) versus total energy ($E$) spectrum obtained from the data collected by the PRISMA IC, along with the polygonal gates used to select different ion species and their corresponding identification.

### 3.1.3 Trajectory reconstruction

In the next step, all the information gathered from each detected event is used to reconstruct the trajectory of the recoiling ion and extract essential quantities for identifying its charge state and mass. This trajectory reconstruction process relies on the position information obtained at the entrance and at the focal plane positions, along with knowledge of the magnetic field intensity in the quadrupole and dipole magnets. The trajectory reconstruction starts by assuming the ion's path begins at the center of the target, allowing calculation of the entrance direction. Using equations of motion for a charged particle in a magnetic field, the path and magnetic rigidity ($B\rho$) in the dipole magnet, with $\rho$ the curvature radius, and the full length of the ion path ($L$) are estimated. The trajectory is assumed to be planar in the horizontal plane during this process.

The velocity of the ions $\beta = v/c$ is then calculated as:

$$\beta = \frac{L}{ToF \cdot c}. \tag{3.6}$$

Using that inside the dipole

$$B\rho = \frac{p}{q}, \tag{3.7}$$

and the relativistic expression for the momentum

$$p = \frac{mv}{\sqrt{1-\beta^2}}, \tag{3.8}$$

one gets

$$\frac{A}{q} = \frac{B\rho}{\beta} \cdot \sqrt{1-\beta^2} \cdot const. \tag{3.9}$$

The velocity of the ions entering PRISMA is of the order $\beta \sim 10\%$, hence, $\sqrt{1-\beta^2} \approx 1$. In this situation, the $A/q$ ration can be calculated as:

$$\frac{A}{q} = \frac{B\rho}{L} \cdot ToF \cdot const. \tag{3.10}$$

### 3.1.4 Charge state identification

The charge state, $q$, identification process involves examining the kinetic energy ($E$) versus $\rho\beta$ matrix for each Z value, as:

$$B\rho \cdot v = \frac{p}{q} \cdot v \approx \frac{mv^2}{q} = \frac{E}{q}, \tag{3.11}$$

$$\Rightarrow E \propto q \cdot \rho\beta. \tag{3.12}$$

The different charge states appear as diagonal structures, as depicted in Figure 3.4. Polygonal cuts are set in the matrix to identify the different charge states. The charge values are assigned based on calculations determining the most intense charge state.

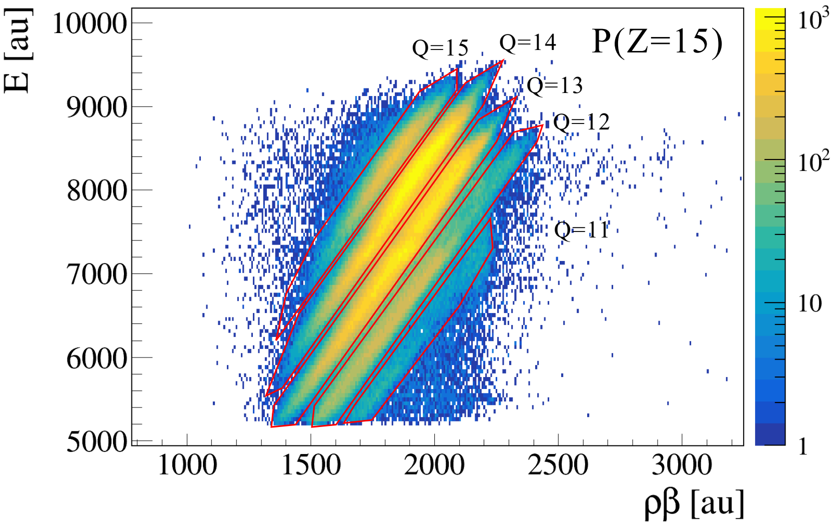

Figure 3.4: Polygonal gates set on the $E$ versus $\rho\beta$ matrix for the identification of the charge states of the P channel.

### 3.1.5 Mass calibration

Gating on $Z$ and $q$, a preliminary mass spectrum can be obtained. However, to retrain the real mass values, a mass calibration is performed in two steps.

First, for each $Z$, a linear calibration is performed on the $A/q$ peaks of each $q$-gated uncalibrated $(A/q)$ spectrum.

$$\mathrm{Mass} = a_Z \left(\frac{A}{q}\right)_{uncal} \cdot q^* + b_Z \tag{3.13}$$

Then, the charge $q^*$ multiplying the $(A/q)$ term is replaced by an effective charge value which is calculated for every $Z$ and $q$ as:

$$q^* = \frac{1}{N}\sum_{i=1}^{N} \frac{A_i}{(A/q)_i}, \tag{3.14}$$

with $N$ being the number of peaks used in the calculation of the effective charge and $(A/q)_i$ being the calibrated $A/q$ value of the centroid of the peak.

This calibration process leads to the mass spectrum in Figure 3.5. Due to instabilities in the raw ToF signal during the experiment, the calibration process had to be repeated three times. The final mass resolution achieved is $\Delta A/A \sim 1/70$.

The relative population of the ion species in the mass spectra seems in good agreement with previous measurements, reported in [34]–[37].

## 3.2 Partial efficiencies of PRISMA

The efficiency of the components of PRISMA was only evaluated with respect to the global trigger of the acquisition. The values provided in Table 3.2 correspond to the ratio of events in which the MCP position, ToF value, or MWPPAC position were measured, relative to the total number of trigger events, given by the MWPPAC cathode. For a measurement of the MCP position to be deemed valid, the data point must fall within a user-defined 2D polygonal gate, established to exclude noisy events. Similarly, the measurements of ToF and MWPPAC position are considered valid only when their respective signals fall within predefined threshold ranges.

A comparison among the values obtained for different $Z$ values shows that the efficiency of all the detectors decreases for the lighter fragments. This phenomenon can be attributed to the fact that PRISMA demonstrates its optimal performance in detecting heavier masses, typically those with $A \gtrsim 60$.

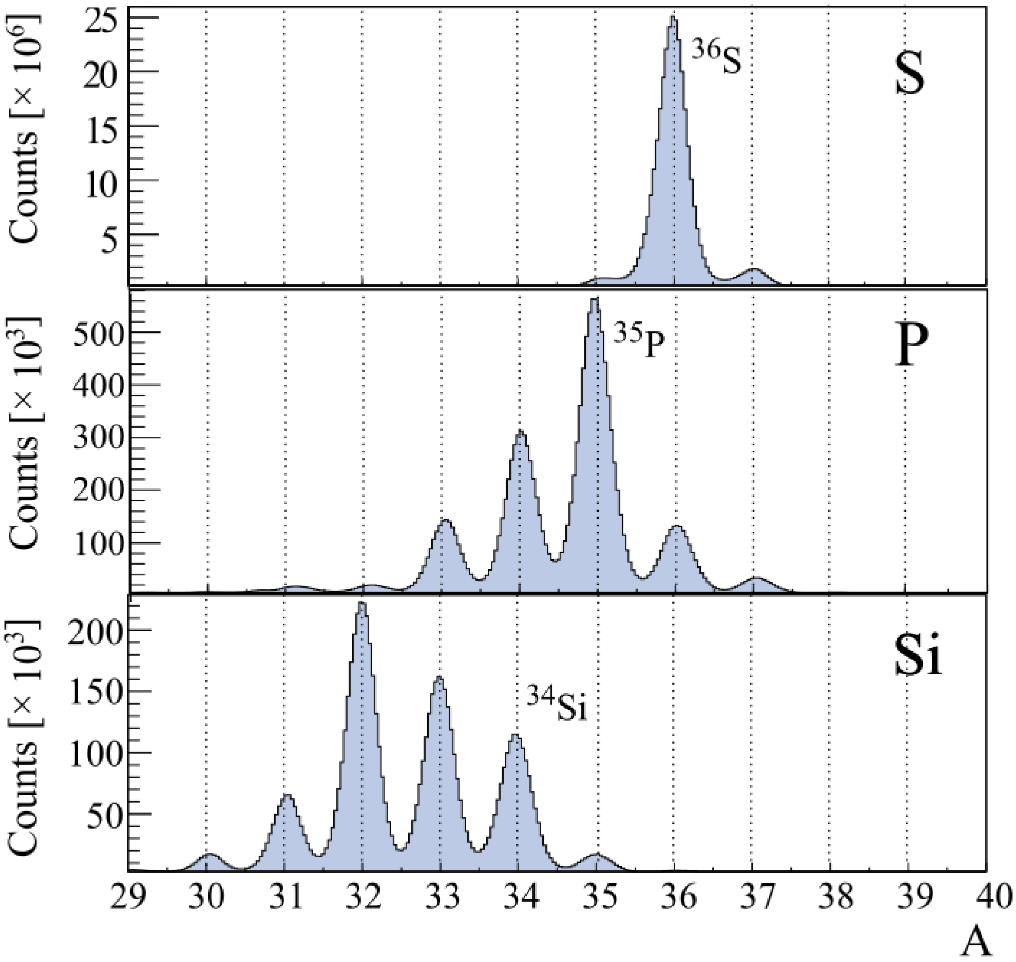

Figure 3.5: Experimental mass spectra for sulfur, phosphorus and silicon nuclei. The isotopes of interest are labelled in each spectrum.

Table 3.2: Partial efficiencies of PRISMA. The values are determined as the ratio of events in which the MCP position, ToF value, or MWPPAC position were measured, relative to the total number of trigger events, given by the MWPPAC cathode. The usual efficiencies for each of the signals is provided between brackets in the first row.

| **Z** | **MCP efficiency [80%]** | **ToF efficiency [85%]** | **MWPPAC efficiency [90%]** |
|---:|---:|---:|---:|
| S (16) | 81.0267 | 85.3695 % | 95.0936 % |
| P (15) | 78.251 | 82.3986 % | 93.9292 % |
| Si (14) | 75.6866 | 79.361 % | 88.8927 % |
| Al (13) | 72.9378 | 75.7002 % | 81.2404 % |
| Mg (12) | 67.2531 | 69.537 % | 73.642 % |

## 3.3 AGATA Analysis

An overview of the detector is provided in Section 2.2. This section outlines the calibration process for the AGATA detectors (presorting stage). The AGATA data-flow makes use of a set of actors [20], listed in in Figure 3.6. Each actor has a distinct role in reading, processing, or writing the data to files. During offline analysis, the NARVAL emulator Femul is used to reprocess (replay) the experimental data. Further details on the data processing can be found in References [38], [39]. The data is processed in two levels: the *local level* and the *global level* processing.

The local level processing involves the reconstruction of the position and energy deposition through the use of Pulse Shape Analysis (PSA) algorithms. Initially, raw data is decoded from all channels (36 segments + 2 cores per crystal) to reconstruct energy and time signals. Channel-by-channel energy spectra are calibrated using data from a calibration source, such as $^{60}$Co or $^{152}$Eu. At this stage, additional optimizations or corrections, such as crosstalk or neutron damage corrections, can be applied when needed.

In the *global level processing* step, data processed individually in the Local level is combined to reconstruct $\gamma$-ray trajectories using a tracking algorithm. Individual interactions in AGATA crystals are grouped and assembled with complementary detector events (PRISMA in this case). Both processes rely on timestamps, enabling event selection within chosen timestamp or *coincidence* windows.

### 3.3.1 AGATA-PRISMA coincidence peak selection

Thanks to the A and Z identification provided by PRISMA, specific events can be selected and it is possible to construct a $\gamma$ spectrum in coincidence with a particular recoling ion-species, or transfer channel. This selective approach allows for the study of $\gamma$ rays emitted by the two nuclei produced in the binary reaction.

The data from both detectors can be merged based on timestamps, and during replay the events falling within a $\sim 1\,\mu$s window as considered as part of a single event. However, for the purpose of distinguishing between background and prompt events, a significantly narrower time coincidence window of 100 ns was defined. This more restricted window, set during the analysis phase between 100 ns and 200 ns, is illustrated in Figure 3.7.

To perform the Doppler correction for each channel, two separate processes are carried out: one for the beam-like ion entering PRISMA and another for the heavier binary partner. For the beam-like partner, the relevant parameters, i.e. the velocity and the relative angle between the ion and the detected $\gamma$ ray, are directly measured. The reconstruction of the binary partner's kinematics involves considering the reaction process, energy losses in the target and degrader, and the emission angle of the beam-like ion.

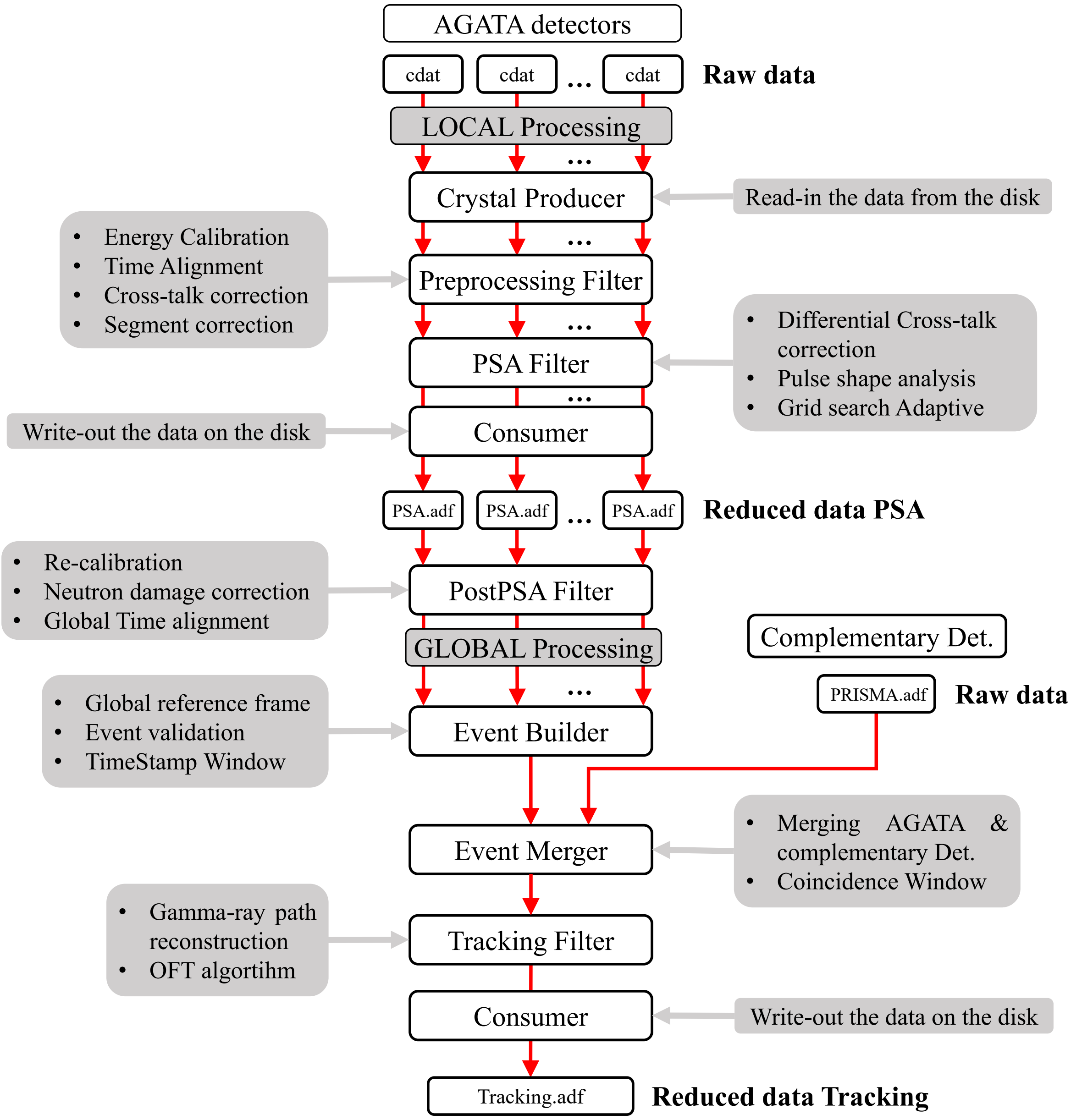

Figure 3.6: Structure of the AGATA data processing with a complementary detector. The data is processed in two differentiated steps: the Local and the Global levels (see text for details). The involved tasks in each level are indicated in boxes with a brief description of their tasks pointed with the grey arrows. The red arrows indicates the direction of the data flow. Taken from [28].

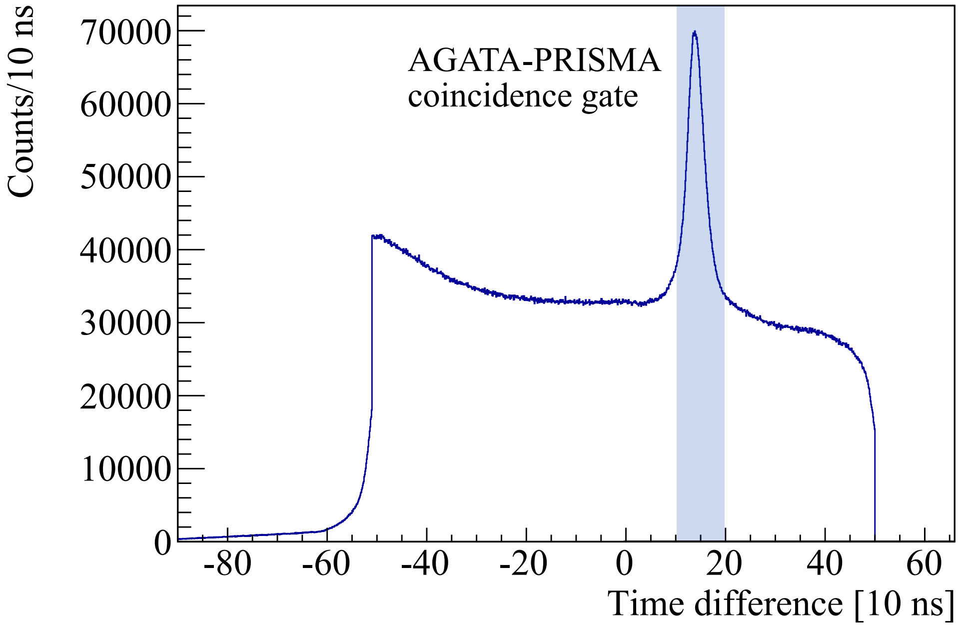

Figure 3.7: Selection of the AGATA-PRISMA coincidence gate.

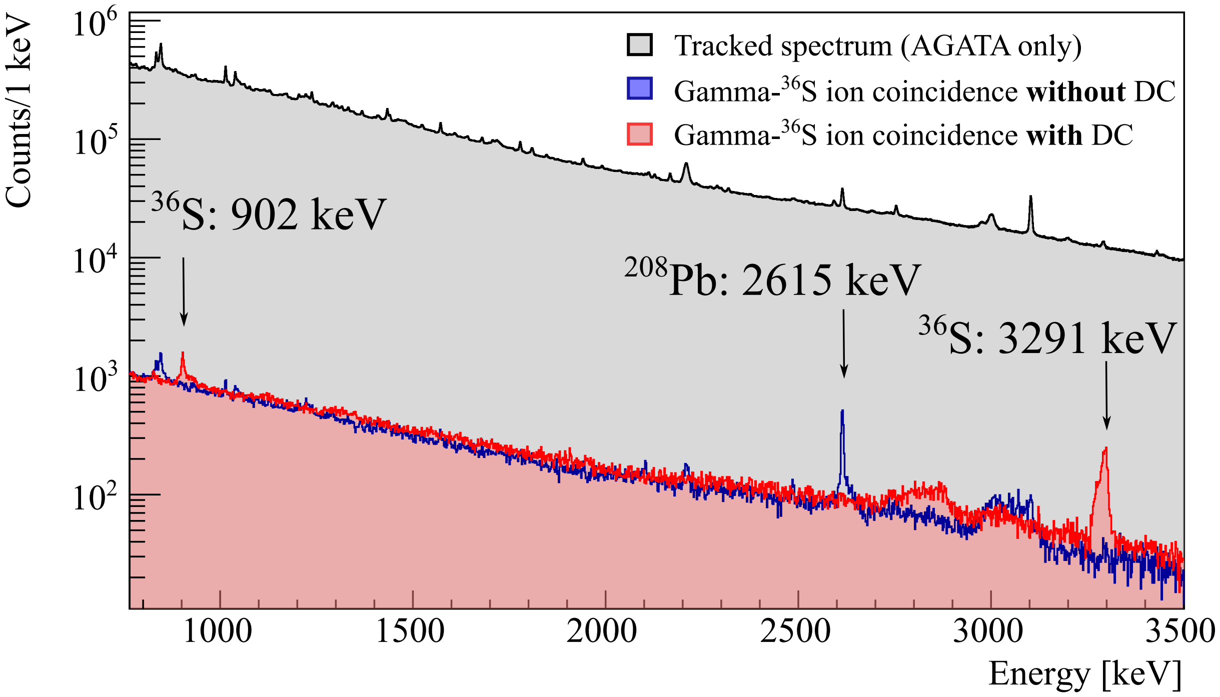

Figure 3.8: Comparison between the AGATA $\gamma$-ray spectra before applying the $^{36}$S mass gate (gray) and after (red and blue). The blue spectrum corresponds to the spectrum obtained when not applying the Doppler correction, while the red one is obtained when Doppler correcting for the beam-like species, based on the PRISMA event-by-event velocity vector measurement. As the binary partner, $^{208}$Pb is very heavy compared to $^{36}$S, the recoiling velocity of $^{208}$Pb $\beta \ll 4\%$, and hence one can identify some transitions corresponding to the binary species in the non Doppler-corrected spectrum.

### 3.3.2 AGATA energy resolution

A remarkable feature of HPGe detectors is their high energy resolution, particularly when employed in $\gamma$-ray spectroscopy, in contrast to the resolution of scintillator detectors [30]. At the data processing stage, the AGATA settings are optimized to correct for effects that could possibly worsen the energy resolution, as highlighted in Section 4.1.

The experimental resolution can be evaluated by measuring the Full Width Half Maximum (FWHM) of the $\gamma$-ray peaks, which follows the empirical trend:

$$\mathrm{FWHM}(E_\gamma) = \sqrt{a + bE_\gamma}, \quad a = 5.57(7)\ \mathrm{keV}^2, \quad b = 4.9(1) \times 10^{-3}\ \mathrm{keV}. \tag{3.15}$$

The energy resolution is defined as

$$R(E_\gamma) = \frac{\mathrm{FWHM}(E_\gamma)}{E_\gamma}. \tag{3.16}$$

The experimental resolution was calculated by fitting the peaks on a $^{152}$Eu source data set. The results are displayed in Figure 3.9. The resolution is best at energies below $\sim 500$ keV, where it is of $\sim 4‰$. At higher energies the energy resolution becomes worse, and stabilizes at values of $\sim 1‰$.

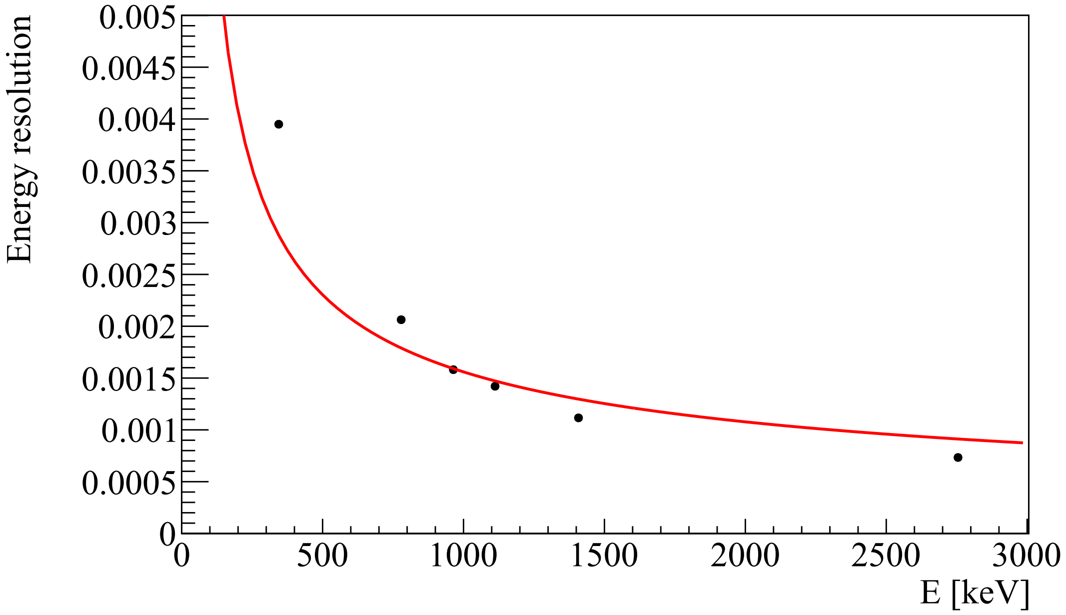

Figure 3.9: Measured energy resolution as a function of the peak energy. The values are measured from the peaks in the $^{152}$Eu source spectrum. The trend line corresponds to a fit with $R(E_\gamma) = \sqrt{a \cdot E_\gamma + b}/E_\gamma$.

## 3.4 Doppler correction optimization

The PRISMA detector offers a significant advantage in in-beam $\gamma$-ray spectroscopy by providing the ability to measure the atomic number ($Z$), mass number ($A$), and velocity ($\vec{\beta}$) of the recoiling ions. This capability is crucial for performing a Doppler correction. In the ion rest frame, the $\gamma$ ray is emitted with the characteristic energy of the transition. However, in the laboratory frame, the $\gamma$-ray energy experiences a shift due to the Doppler effect, which depends on two main factors: the velocity of the recoiling ion, $\beta$, and the angle of $\gamma$ emission with respect to the moving direction of the emitter, $\theta$.

The high position resolution of both the PRISMA and AGATA detectors provides unique features for accurately correcting the Doppler shift of the spectra. However, because the correction heavily relies on the velocity measured by PRISMA and the relative angles between the detectors, an optimization process is usually necessary during the analysis step. This ensures that the energy of the $\gamma$ rays appears at the correct energy in the Doppler-corrected spectra and helps reduce the FWHM of the peaks emitted after target and degrader.

In order to optimize the Doppler correction, a suitable reference transition or set of transitions must be chosen. It is important that these transitions provide sufficient statistics and do not exhibit any lineshapes caused by the Doppler Shift Attenuation Method (DSAM) broadening. In this study, the 646.2 keV transition in $^{37}$S was selected for its high statistics and measured state lifetime of 193(4) ps [40], which is well above the sensitivity of the DSAM and ensures no tails are expected due to energy loss in the degrader.

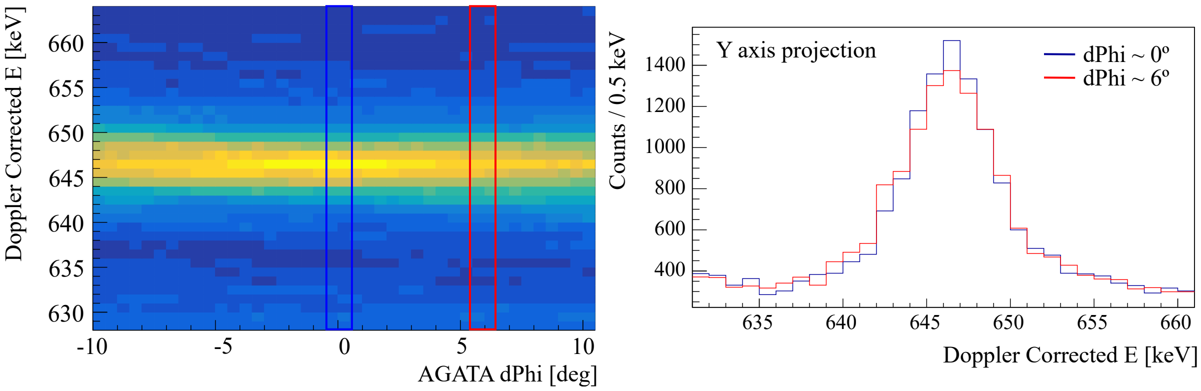

Figure 3.10: Comparison between the optimized (blue) and the non-optimized (red) azimuthal position of the AGATA array. The FWHM of the peak increases as one moves away from the selected optimal value, resulting in a worsening of the energy resolution.

The optimization process involved two main steps: first, the ToF of the ions was adjusted to ensure that the $\gamma$-ray transition appeared at the correct rest-frame energy. Next, various values for the AGATA $\theta$ and $\phi$ angles, as well as the AGATA z-offset, were tested, to determine the correct position of the array. The final optimized values for the angles and AGATA z-postion offset were selected based on the ones that minimized the FWHM of the peaks. Figure 3.10 illustrates the comparison between spectra as a function of the azimuthal angle, $\phi$, showing that the FWHM increases as one moves away from the selected optimal value.

Figure 3.11 shows a comparison of the experimental 646.2 keV peak before and after the optimization process. The final peak has a FWHM of 5.2 keV, which was considered sufficient as the observed DSAM tails are $\sim$ 50 keV.

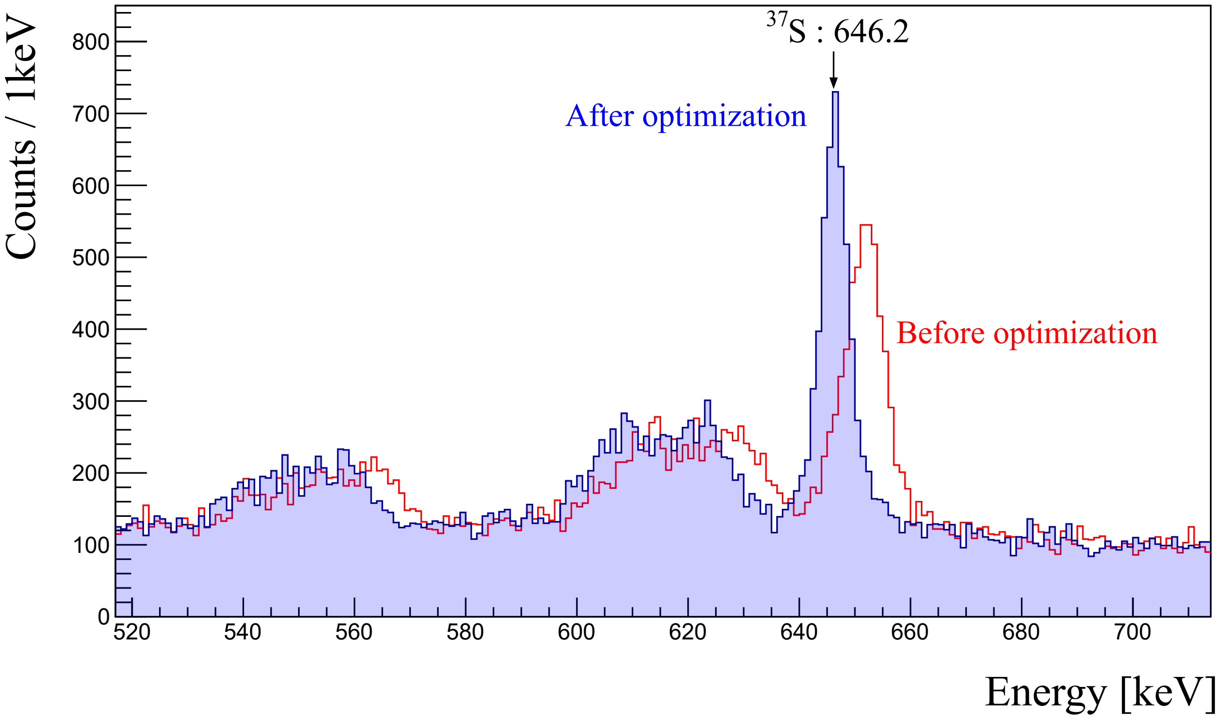

Figure 3.11: Comparison of the experimental 646.2 keV peak in $^{37}$S before and after the optimization process.

# 4

# Simulation and lifetime estimation

The primary objective of this experiment is to determine the lifetimes of specific excited states in $^{34}$Si and $^{35}$P. This can be achieved by comparing experimental Doppler-corrected peak shapes with those derived from a realistic Monte Carlo simulation.

For this purpose, a simulation software package provided for AGATA and complementary devices was used [41]. The software is based on `GEANT4` [42], and was designed to generate simulated $\gamma$-ray spectra, mimicking the geometry, crystal configuration, and set up performance during the experiment. Moreover, it allows for the generation of particle events and the simulation of nuclear reactions. When particle detectors such as PRISMA are present, the simulation can be set to reproduce Doppler-corrected spectra under the same conditions as the in-beam experiment.

Nevertheless, in order to ensure agreement between the experimental data and the simulation, the simulation needs to be specifically adapted to reproduce the detector resolutions and account for velocity smearing effects. This chapter focuses on the simulation optimization, which was performed using the AGATA simulation software and the extraction of the lifetime of the $2_1^+$ state in $^{36}$S and of the $3/2^+$ state in $^{35}$P, which has not been previously reported in the literature.

## 4.1 Optimization of the simulation

This section covers the diverse factors integrated into the simulation to realistically reproduce the experimental conditions.

### 4.1.1 Detector geometry

During the experiment, certain crystals (05A, 05B, and 05C) were absent in the set-up, and some others (07B and 14A) were removed during the analysis step. To adapt the simulation, the missing crystals were directly excluded from the simulated set-up, while the ones removed during analysis were retained in the simulation but removed at the tracking step. This approach allows simulated $\gamma$ rays to interact with the germanium of the 07B and 14A detectors, but their signals are not processed further, similar to the experimental conditions. A comparison between the tracked experimental and simulated interaction points is provided in Figure 4.1, demonstrating that the positions of the detectors in the simulation match the ones of the real set-up.

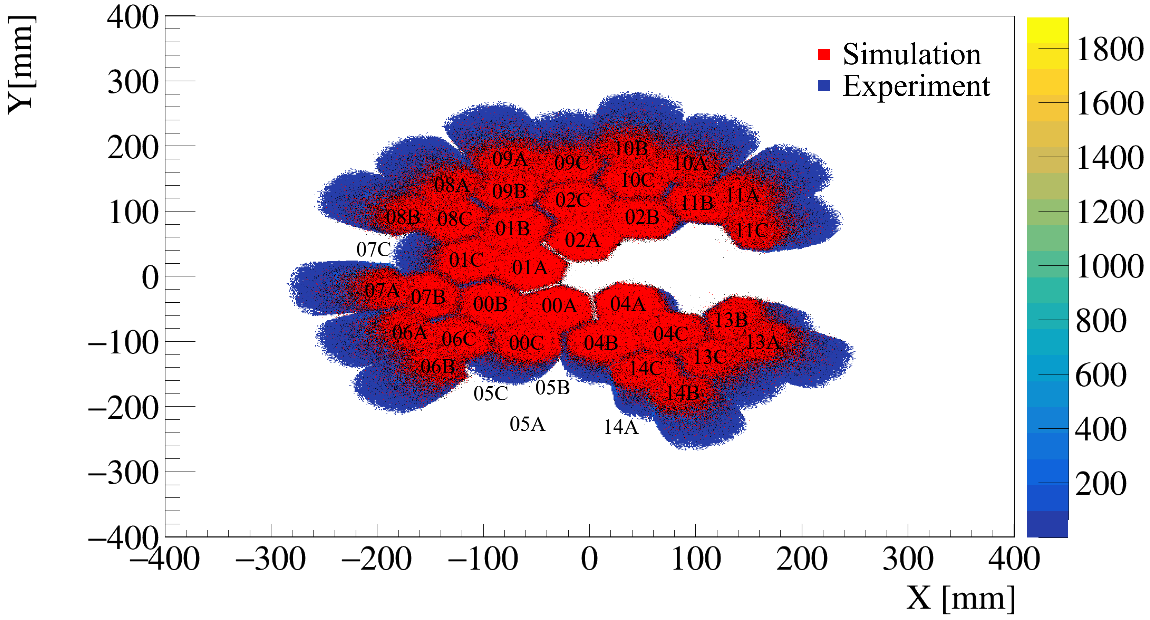

Figure 4.1: Comparison between the distributions of the experimental and simulated tracked interaction points.

### 4.1.2 Resolution

In Doppler Shift Attenuation Method (DSAM) measurements, realistically reproducing the resolution of the detectors is essential, given that the determination of lifetime relies on the peak shape. As detailed in Section 3.3.2, the energy resolution of Advanced GAmma Tracking Array (AGATA) depends on the energy of the $\gamma$ rays, with a gradual increase of the Full Width Half Maximum (FWHM) at high energies. To incorporate this effect in the simulation, we introduced a smearing effect of the $\gamma$ ray energies.

The energy of the $\gamma$ rays was smeared after tracking according to the equation

$$E'_{\gamma} = E_{\gamma} + \epsilon(\mu_E, \sigma_E),$$

where $\epsilon(\mu_E, \sigma_E)$ is a random number sampled from a Gaussian distribution with mean $\mu_E = 0$ and variance $\sigma_E = 2.35$ FWHM$(E)$. The function FWHM$(E)$ is the empirical dependence of the FWHM on the energy of the $\gamma$ rays, deduced from an experimental run with a $^{152}$Eu source.

Then, to compare the Monte Carlo results with the experimental data, we simulated a $^{152}$Eu source placed in the target nominal position. The FWHM of the simulated peaks was extracted by employing the same fitting procedure as applied to the experimental dataset. A single 2755 keV transition was included in the simulation to investigate the trend at higher energies. Figure 4.2 compares the experimental and simulated data. The red line indicates the empirical trend

$$\mathrm{FWHM}(E) = \sqrt{a + bE_\gamma}, \quad a = 5.57(7), \quad b = 4.9(1) \times 10^{-3}; \tag{4.1}$$

retrained from the experimental data. The simulated data points exhibit a comparable trend to the experimental counterpart. It was also observed that the experimental data exhibited some minor tails, which were not considered at this stage.

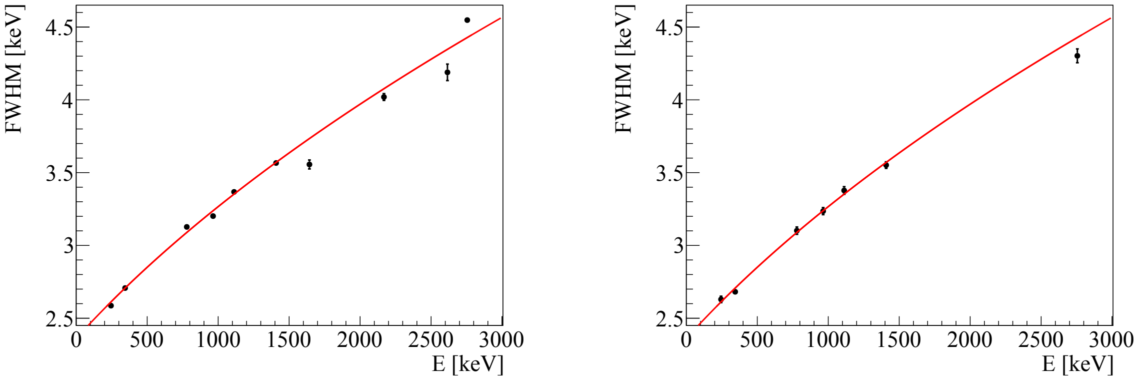

(a) Experimental data.

(b) Simulated data.

Figure 4.2: Comparison between the energy dependence of the FWHM of the peaks of a non-Doppler corrected experimental (left) and simulated (right) $\gamma$-ray spectrum.

### 4.1.3 Velocity smearing

The information of the velocity of the ions measured by PRISMA is employed for the event-by-event Doppler correction of the $\gamma$-ray spectrum. The finite resolution of PRISMA translates into a broadening of the peaks in the Doppler-corrected $\gamma$-ray spectra. Thus, in addition to the energy smearing effects discussed in Section 4.1.2, the recoiling velocity is smeared according to

$$\beta' = \beta + \tilde{\epsilon}(x_0, \gamma), \tag{4.2}$$

with $\tilde{\epsilon}$ a random number sampled from the probability distribution function

$$f(x) = \frac{\gamma}{\pi\,\left[1 + (x - x_0)^2\right]} \tag{4.3}$$

centered around $x_0 = 0.0015$ and scaled by a factor $\gamma = 0.015$. This distribution was selected for the smearing of the velocity of the ions, instead of a Gaussian, because the $\gamma$ peak obtained when applying the Doppler correction, using $\beta'$, reproduced better the shape of the 646 keV transition in $^{37}$S. It is worth noting that this transition was chosen due to its lifetime falling outside the experimental sensitivity range, resulting in no DSAM tails. Refer to Figure 4.3 for a visual comparison of the experimental and simulated peaks.

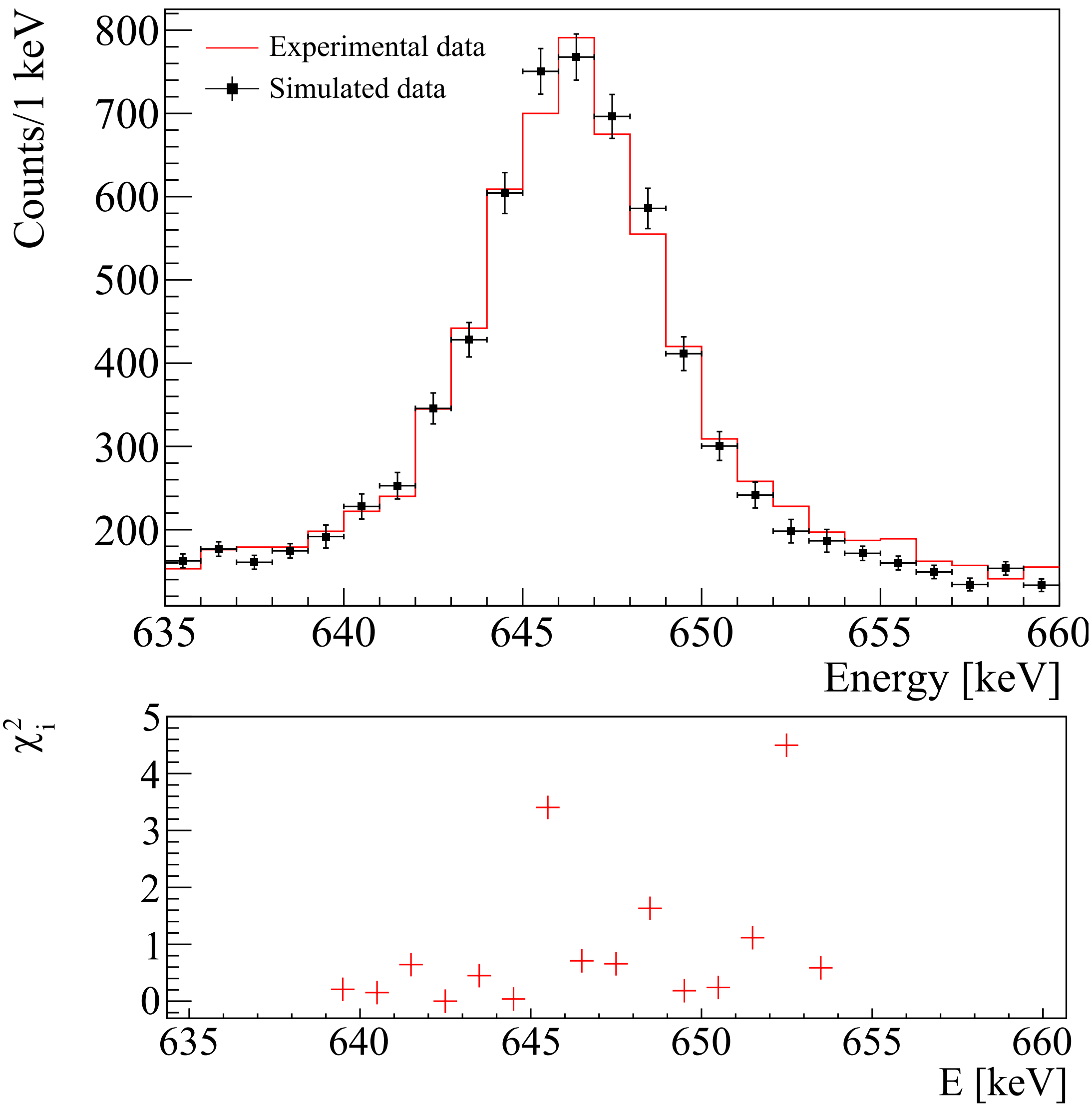

Figure 4.3: Comparison between the experimental and the simulated 646 keV peak in $^{37}$S. In the plot below the $\chi^2$ residuals are provided, which were used as a test to determine the best-suited smearing probability distribution function and its parameters.

### 4.1.4 Background generation

For computational optimization purposes, the background generation was added separately to the `GEANT4` simulation. In the `GEANT4` simulation, only the single transition of interest was generated. Then, after applying the tracking and smearing effects, an exponential background was added to the spectra.

The background is generated by sampling from an exponential distribution, with its parameters derived from experimental data. This background addition was limited to a narrow energy range around the transition's energy, spanning only a few hundred keV. This strategy allowed us to drastically reduce the time required to generate the simulated dataset. Moreover, the number of background events added was set to be consistent with the peak-to-background ratio of the experimental data.

## 4.2 Lifetime estimation of the $^{36}$S $2_1^+$ state

As a first step, the lifetime of the $2_1^+$ state in $^{36}$S was extracted, which decays to the ground state via an $E2$ transition emitting a 3291 keV $\gamma$ ray. The lifetime of this state, $\tau = 120(10)$ fs, has been previously reported in the literature in Reference [43]. It was measured in a Coulomb excitation experiment using a similar experimental technique. The independent measurement of the lifetime of that state allowed for the identification of potential systematic effects which may also arise when measuring the unknown lifetime of other states. This channel was initially selected due to the high amount of statistics.

### 4.2.1 Line-shape analysis method

The lifetime of the state is extracted by comparing the shape of the peak of the experimental dataset with a set of `GEANT4` simulations generated following the method explained above. To compare both and establish which lifetime value reproduces best the experimental data, the least-$\chi^2$ method was used.

The least-$\chi^2$ method is a statistical method frequently used in fitting procedures to determine the *goodness of a fit*, to test hypotheses, and for parameter optimization [44]. This is done by minimizing the sum of the squared vertical distances (residues) between the data points and the fit. Given a set of $N$ experimental data points $(x_i, y_i)$ and an uncertainty $\sigma_i$, with a fitting function $f(x_i)$ defined by $M$ free parameters $\theta_k$, the $\chi^2$ quantity is defined as:

$$\chi^2 = \sum_{i=1}^{N} \left( \frac{y_i - f(x_i)}{\sigma_i} \right)^2 .$$

In this analysis, however, it is required to compare two sets of binned data, namely the experimental and the simulated one. To compare them, we used the *Pearsons's* $\chi^2$ *test*, which consists in minimizing the quantity:

$$\chi_P^2 = \sum_i \frac{(n_i - y_i)^2}{y_i},$$

where $n_i$ is the number of events in the $i$-th bin of the simulation. This assumes that the experimental data follows a Poisson distribution and hence, $\sigma_i = \sqrt{y_i}$. To compare both histograms, the simulated histogram must be normalized such that both histograms contain the same total number of counts in the range of bins where the $\chi_P^2$ quantity is calculated.

Moreover, it is important to note that in this test the variance of the simulated data is neglected, which implies that the number of events simulated must be big enough such that statistical fluctuations due to the simulation are not significant. We decided to run the `GEANT4` simulation with $10^7$ events for the single $\gamma-$transition (before background addition). This yielded approximately 500 times more events compared to the experimental dataset, and the approximate uncertainties for the experimental and simulated datasets are $\sim$ 20% and 1%, respectively.

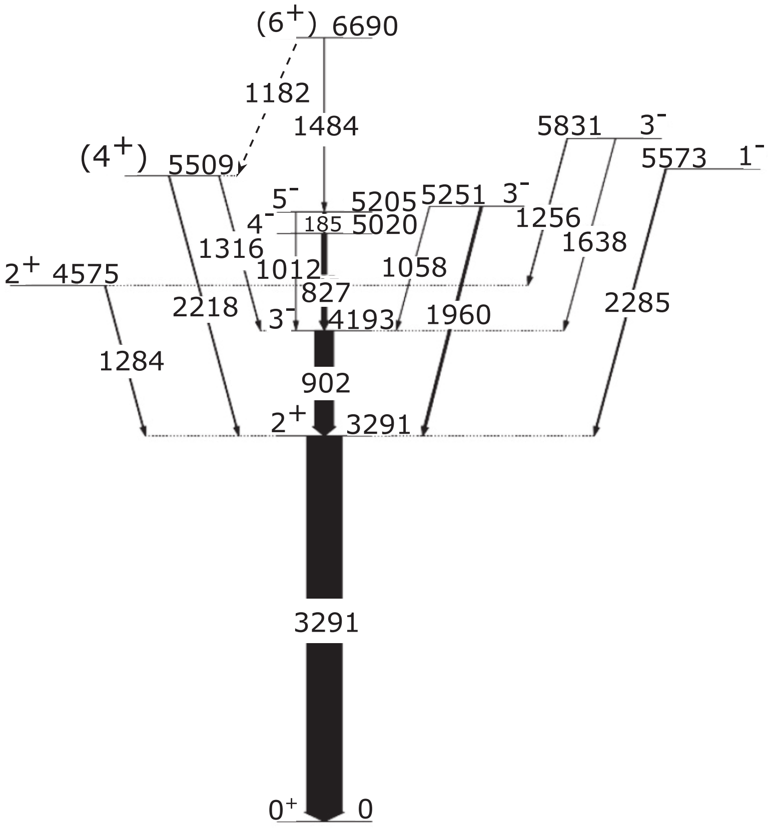

Figure 4.4: $^{36}$S level scheme reconstructed from a $^{36}$S on $^{208}$Pb reaction. Taken from Reference [37].

### 4.2.2 Preliminary estimations and TKEL selection

Our first lifetime estimates overestimated the state's lifetime compared to previous measurements. While the lifetime reported in the literature is $\tau = 120(10)$ fs [43], our first estimations were of $\tau \approx 150(10)$ fs. The cause of this overestimation was identified as the contribution from the intense $3_1^- \rightarrow 2_1^+$ 901 keV transition (refer to Figure 4.4 and Figure 4.7), which feeds the $2_1^+$ state. The influence of the feeders depends on the branching ratio of the feeding transition, on the population of the higher-lying state, and its lifetime [18]. The previous measurement for the $3_1^-$ state measured a lifetime of 0.9(1) ps, which aligns with the overestimation hypothesis. Moreover, as the lifetime of the $3_1^-$ state is over the experimental range of sensitivity, the 3291 keV $\gamma$ rays emitted from the $3_1^- \rightarrow 2_1^+ \rightarrow 0^+$ cascade occur solely after the degrader, resulting in an in-flight peak component which can be observed in the experimental $\gamma$ ray spectra.

Two methods were attempted to eliminate the feeding effect. The first involved including the feeder transition in the simulation. However, the precise population of the $3_1^-$ and $2_1^+$ states was uncertain, and no significant peak shape changes occurred when varying the $2_1^+$ state's lifetime. The simulation predominantly depended on the $3_1^-$ state's lifetime, which has an error bar comparable to the experiment's sensitivity range.

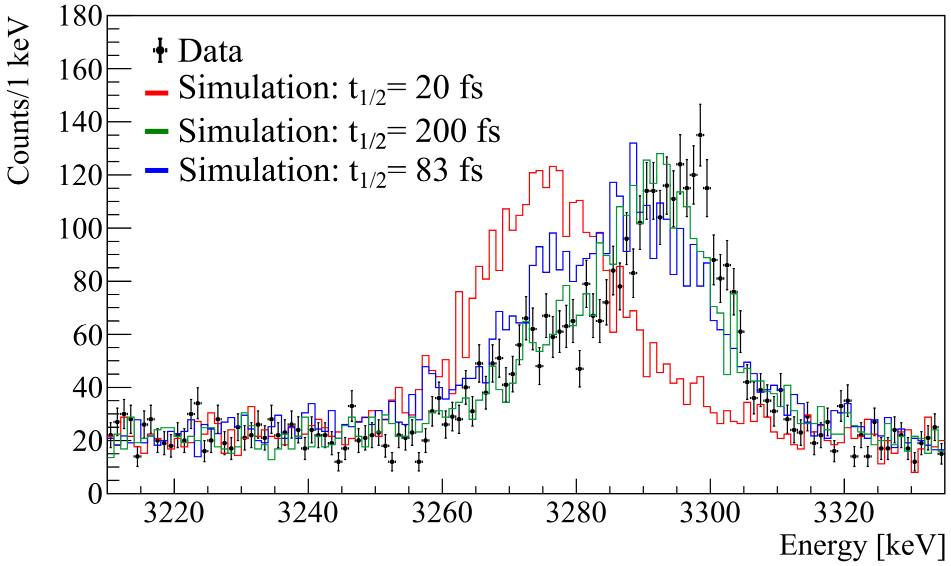

Figure 4.5: Preliminary comparison between the experimental and simulated data, including the feeding from the $3^-$ state. The shape of the peak is better reproduced by the $\tau = 288$ fs ($t_{1/2} = 200$ fs) simulation , which disagrees with the previous measurement of $\tau = 120(10)$ fs ($t_{1/2} = 83(7)$ fs) reported in Reference [43]. The cause of this overestimation was identified as the contribution from the intense $3_1^- \rightarrow 2_1^+$ 901 keV transition, with a measured lifetime of 0.9 (1) ps [43], which feeds the $2_1^+$ state. See text for further details.

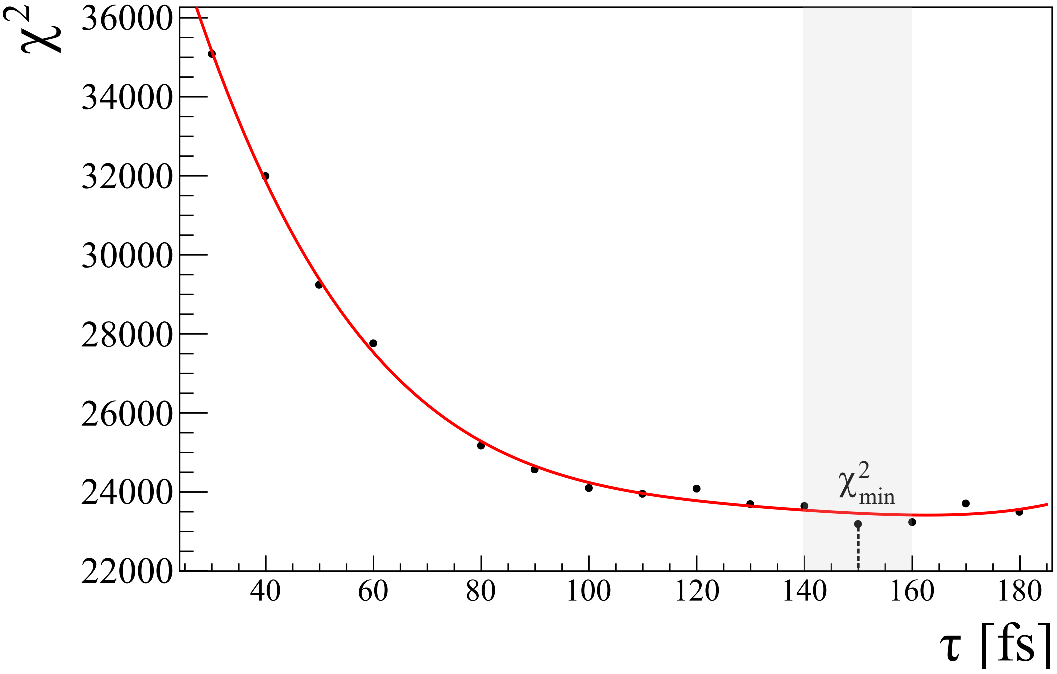

Figure 4.6: Preliminary $\chi^2$ gradient for the determinant ion of the $2_1^+$ $^{36}$S state lifetime. At this stage, no selection on the Total Kinetic Energy Loss (TKEL) spectrum was performed, which resulted in an estimation of $\tau \approx 150$ (10) fs, above the previous measurement of 120 (10) fs reported in Reference [43].

The second approach involved the selection of distinct ranges within the Total Kinetic Energy Loss (TKEL) spectrum. It was observed that the shape of the $^{36}$S 3291 keV peak showed a strong correlation with the TKEL. This stems from the correlation between the TKEL and the excitation energy $E_{ex}$ of the reaction products:

$$\text{TKEL} = E_{ex} - Q_{gs} = E_{ex} - (M_f - M_i)\, c^2 \tag{4.4}$$

The event-by-event information on the TKEL allows us to distinguish between $\gamma$ rays produced by low-lying states, i.e. a direct population of the $2_1^+$ sate, and high-lying states, i.e. the $3_1^- \rightarrow 2_1^+ \rightarrow 0^+$ cascade. Thus, an upper threshold was established on the TKEL spectrum to remove the feeding coming from the $3_1^-$ state. Additionally, the $^{36}$S channel shows a strong contribution from the elastic channel at the lower range of the TKEL spectrum, which leads to an increase in the background level. This effect was partially eliminated by introducing a lower threshold in the TKEL spectrum. Figure 4.7 depicts the three different ranges selected. Yet, it is worth noting that this procedure resulted in a significant reduction of the available statistics, requiring a rebinning of the histogram. The TKEL-gated $\gamma$-ray spectra corresponding to the three ranges highlighted in Figure 4.7 are shown in Figure 4.8. Only the spectrum labeled as (b), where the contribution of the 902 keV transition is minor, was used for the lifetime measurement of the $2_1^+$ state (see Section 4.2.3).

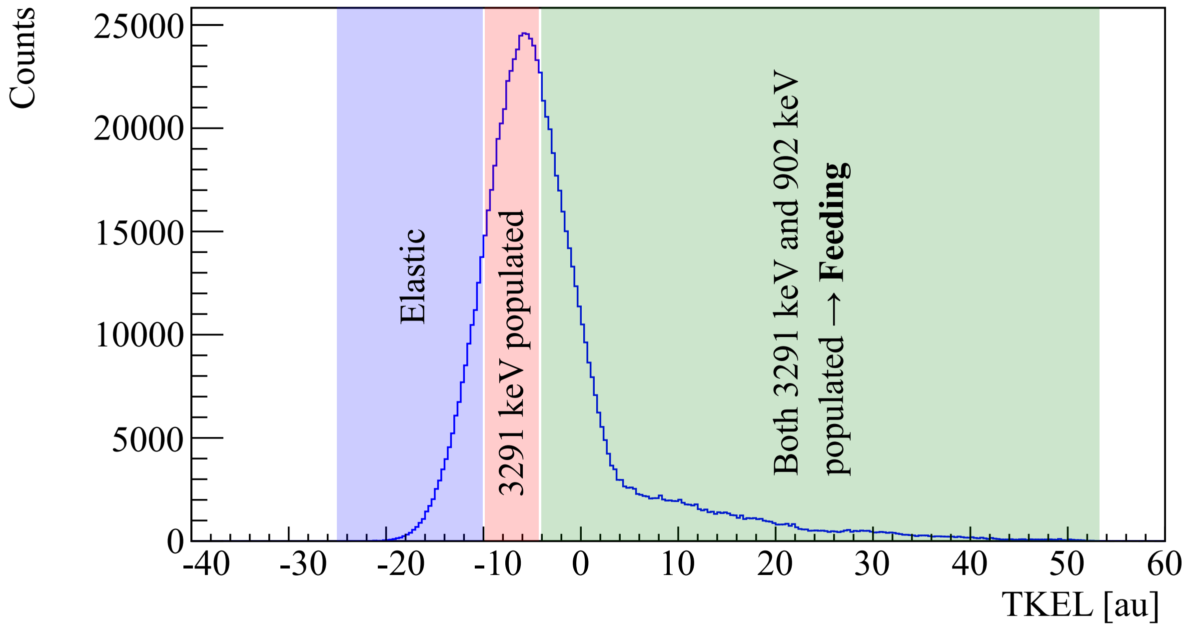

Figure 4.7: Total Kinetic Energy Loss (TKEL) spectrum retrieved from PRISMA on an event-by-event basis. The correlation between the TKEL and the excitation energy of the reaction products allows for the distinguishing of three different ranges. In the lower part of the spectrum, highlighted in blue, the elastic channel dominates, and no $\gamma$-ray peaks of $^{36}$S can be observed. In the intermediate range, the 3291 keV transition is predominantly populated. In the uppermost region, highlighted in green, the population of the $3_1^-$ state, which decays through the emission of a 902 keV $\gamma$ ray results in an overestimation of the $2_1^+$ lifetime due to feeding effects.

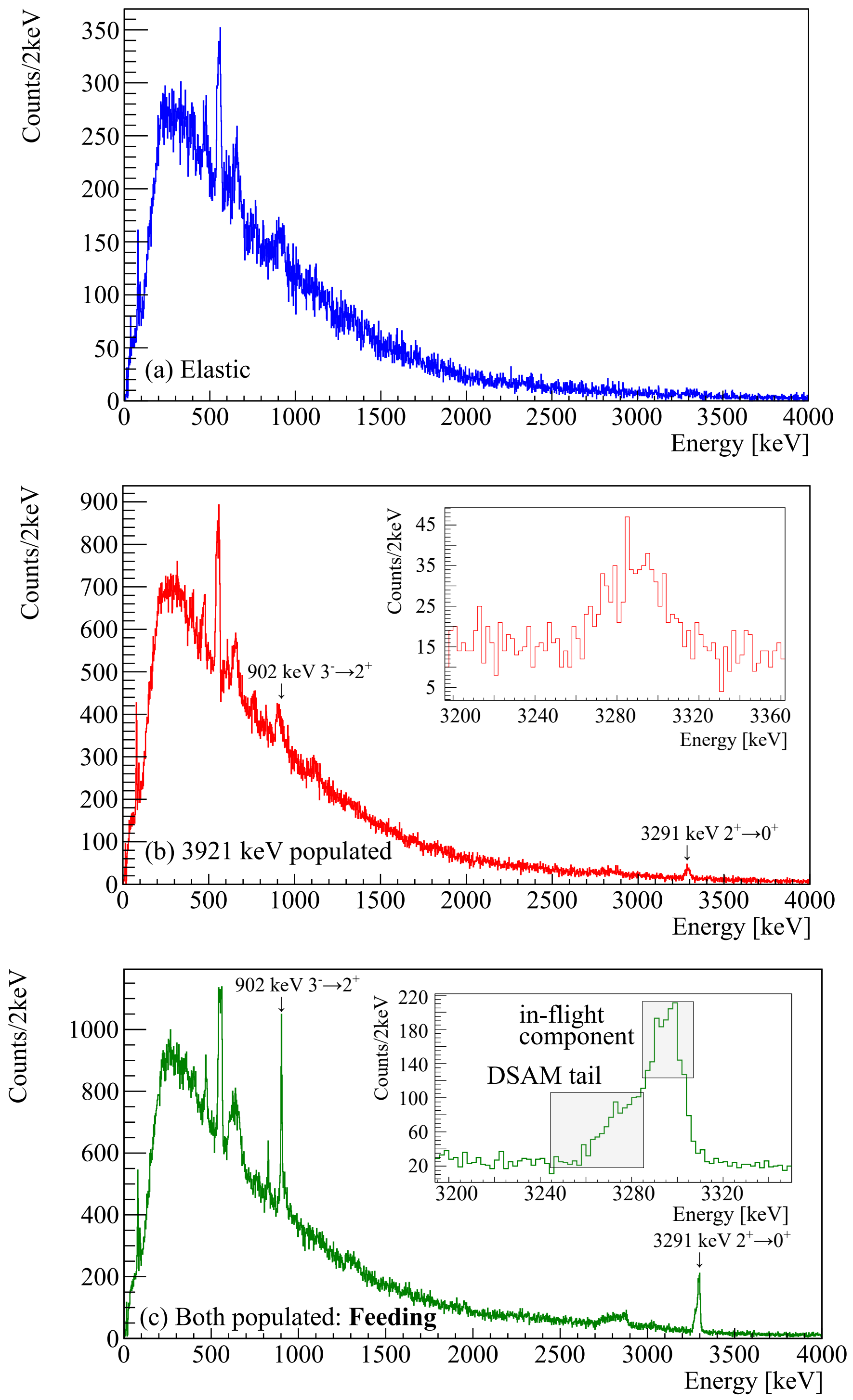

Figure 4.8: The AGATA $\gamma$-ray spectra coincide with $^{36}$S ions by applying the TKEL thresholds depicted in Figure 4.7. (a) In the lower TKEL region, highlighted in blue in Figure 4.7, the spectrum is dominated by the elastic channel, and there are no discernible $^{36}$S $\gamma$-ray transition peaks present. (b) Within the intermediate range, highlighted in red, the 3291 keV peak corresponding to the $2_1^+ \rightarrow 0^+$ transition can be observed. However, the 902 keV peak, responsible for the feeding of the 3291 keV transition, is not intensely observed. (c) In the uppermost region of the TKEL spectrum, both the 3291 keV and the 902 keV peaks are visible, which gives rise to difficulties in precisely determining the lifetime of the $2_1^+$ state, influenced by feeding effects, which result in an overestimation of the lifetime.

### 4.2.3 Lifetime estimation and correlation with the $\gamma$-ray energy

Due to the significant correlation between the measured lifetime and the energy of the $\gamma$ rays, the analysis was extended to determine both two parameters: the $\gamma$-ray energy and the lifetime of the state. While the energy of the transition is established from prior spectroscopic measurements, the precise position of the peak's centroid in the experimental spectra is heavily dependent on the Doppler shift correction.

The lifetime was determined using a 2-parameter minimization, sampling within a range of 3290 keV to 3297 keV with an interval of 1 keV in energy, and from 40 fs to 180 fs with an interval of 10 fs in time. The corresponding energy for the minimum $\chi^2$ was found to be 3295 keV, which yielded an estimated lifetime of $\tau = 100$ fs, with a statistical uncertainty of approximately 10 fs (see text below). Figure 4.10 displays the $\chi^2$ as a function of both energy and lifetime, while Figure 4.11 shows the gradient corresponding to an energy of 3295 keV.

Although the energy of the transition corresponds to 3291 keV, an energy of 3295 keV is consistent with the position of the in-flight peak ($\gamma$ rays emitted after degrader) in the $\gamma$ spectrum. The centroid of the peak was calculated by gating on the region corresponding to the highest TKEL. In this case, the DSAM component of the peak is expected to be suppressed, as the state is mostly indirectly populated by longer-lived states. An alternative method consists of analyzing the $\gamma - \gamma$ coincidence matrix, but this method was not applicable due to the lack of statistics. The inset in Figure 4.9 depicts the region where the TKEL gate was set, as well as the experimental and fitted peak. Despite a slight tail on the left, the in-flight component of the Doppler corrected peak is dominant. When fitting the peak and the background, the centroid energy is 3294.3(6) keV.

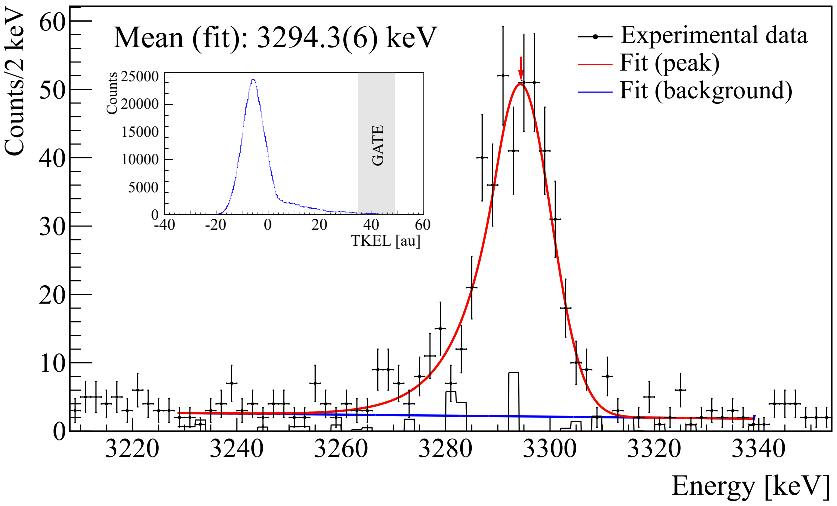

Figure 4.9: 3291 keV peak obtained by gating at the highest region of the TKEL spectrum, displayed on the inset of the figure. The range of the TKEL spectrum was selected to remove the DSAM tail, expected at the left of the peak.

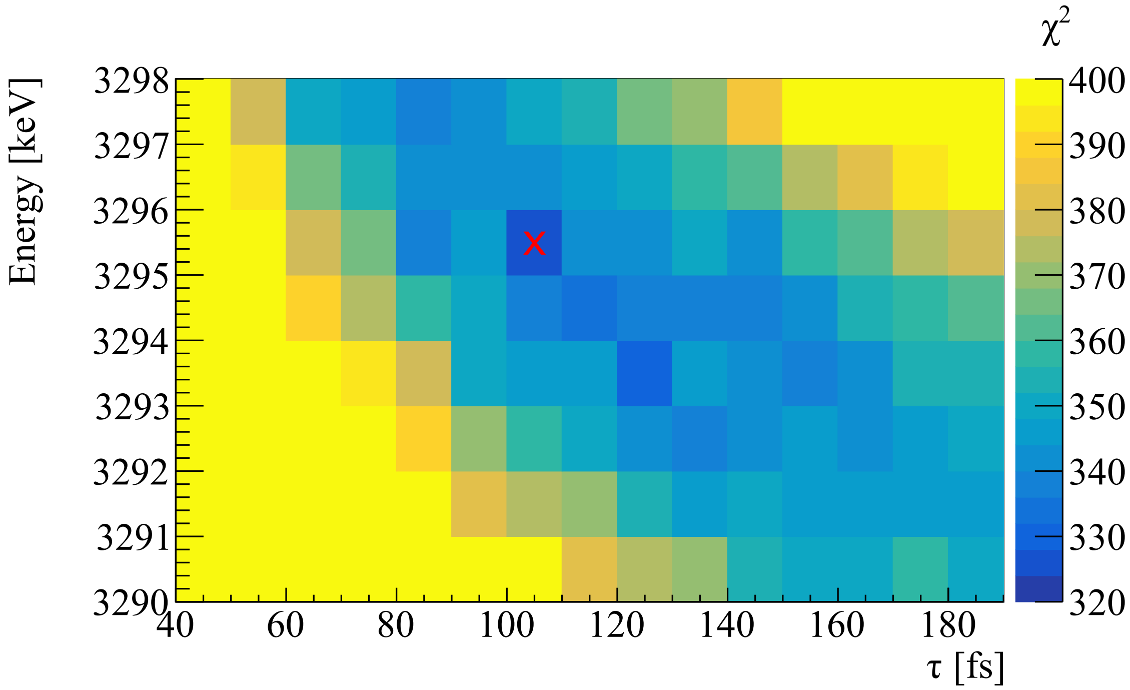

Figure 4.10: $\chi^2$ distribution for the estimation of two parameters: the lifetime of the $2_1^+$ state in $^{36}$S and the energy of the $2_1^+ \to 0^+$ transition, using the Pearson's $\chi^2$ test. The red cross indicates the global minimum of the 2D $\chi^2$ gradient.

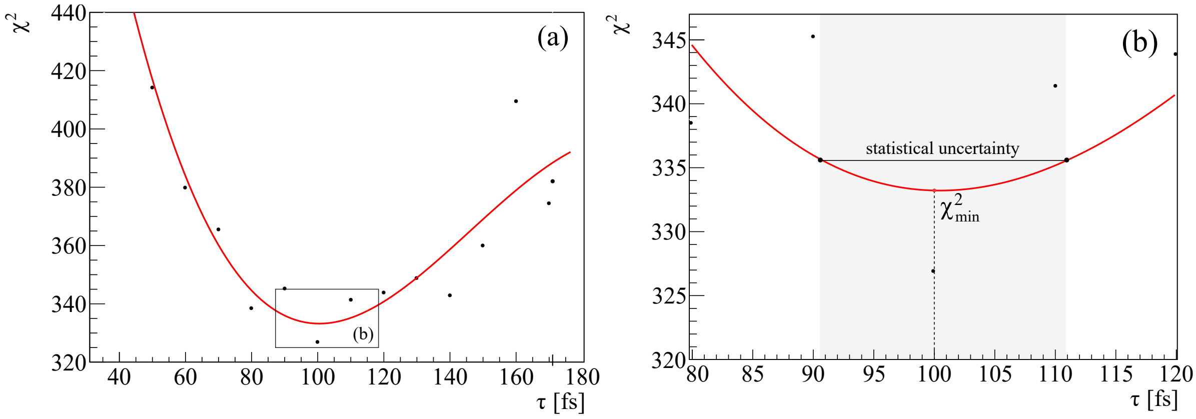

Figure 4.11: $\chi^2$ minimization for the $^{36}$S $2_1^+$ state. (a) The gradient obtained for a $\gamma$ ray energy of 3295 keV was selected as optimal, as it yielded the global minimum of the minimization for the estimation of both the energy of the transition and the lifetime of the state. To avoid the fluctuations of the $\chi^2$, a 4th-degree polynomial fit of the gradient was used for the estimation of the lifetime. (b) The statistical uncertainty was extracted as the range where $\chi^2 \leq \chi^2_{min} + 2.3$ (see Reference [44]). The minimization yielded a value of 100(11) fs.

To estimate the statistical uncertainty, we selected the lifetime interval that satisfies the following condition:

$$\chi^2 \leq \chi^2_{min} + 2.3. \tag{4.5}$$

When estimating two parameters, i.e. energy and lifetime, an increase of $\Delta\chi^2 \leq 2.3$ with respect to the minimum value corresponds to a confidence limit of one standard deviation in the parameters' estimation [44], [45]. However, we believe the statistical uncertainty is underestimated, possibly due to the non-linear nature of our model, and the low amount of statistics in the experimental histogram. This will be further assessed in the future.

Furthermore, the value of $\chi^2_{min}$ ($\sim$ 300), is higher than the expected value for the number of degrees of freedom ($ndf \sim 40$) in the fit. The reason for the high $\chi^2_{min}$ needs to be investigated further. One possible explanation is the shift of approximately 4 keV to the right observed in the peak, in comparison to the actual energy of the transition. This shift may be affecting the shape of the peak and is not properly accounted for in the simulation. There may be other reasons for the high $\chi^2_{min}$ value such as an incorrect representation of the background or the presence of unidentified peaks in the region.

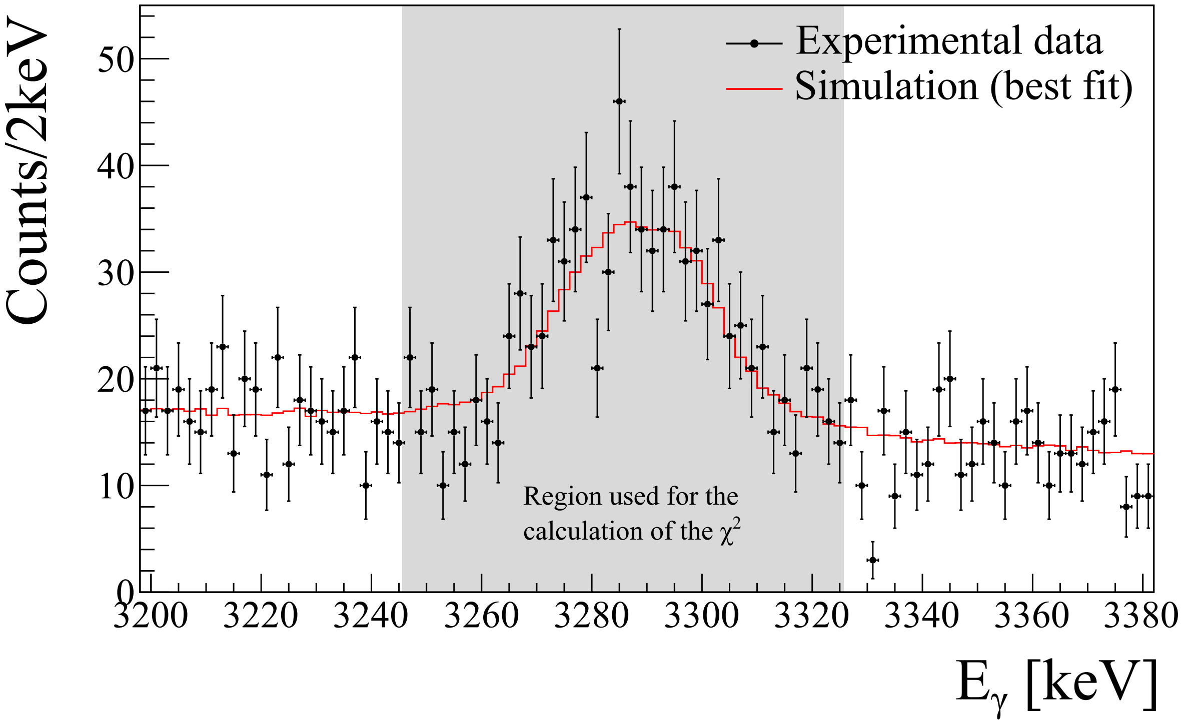

Figure 4.12: Comparison between the experimental peak used for the estimation of the lifetime (TKEL gated), and the best-fitting simulation. The simulation corresponds to an energy of 3295 keV, and a lifetime of $\tau = 100$ fs.

### 4.2.4 Variability of the measurement on the TKEL selection

To remove the effect of the feeding from the $3_1^-$ state on the lifetime estimation, the measurement was performed on a subset of the experimental dataset obtained by gating on the range of the TKEL spectra where the 3921 keV transition was visible, but the 901 keV transition was not intensely populated. However, due to limitations in the TKEL resolution, it was not possible to define precise boundaries for the employed TKEL gates.

To assess the uncertainty introduced by the TKEL selection, six distinct sets of experimental TKEL gated spectra were generated. Each of these sets spanned a slightly different range of TKEL values. The $\chi^2$ gradient which presents the global minimum and is depicted in Figure 4.11, covered a range of $[-9.3, -2.45]$ au in the TKEL spectrum. The other 5 sets spanned the ranges: $[-10.5, -3.5]$ au, $[-10, -3]$ au, $[-9.5, -2.5]$ au, $[-9, -2]$ au, and $[-8.5, -1.5]$ au.

Upon performing this analysis, the calculated lifetimes spread in a range from 80 fs to 100 fs (see Figure 4.13). The maximum difference between the data points was used as an estimation of the overall uncertainty, and it is shaded in gray in Figure 4.13. In the end, the overall uncertainty is estimated at 20 fs, hence the lifetime estimation yields a value of 100(20) fs, which is compatible with previous measurements.

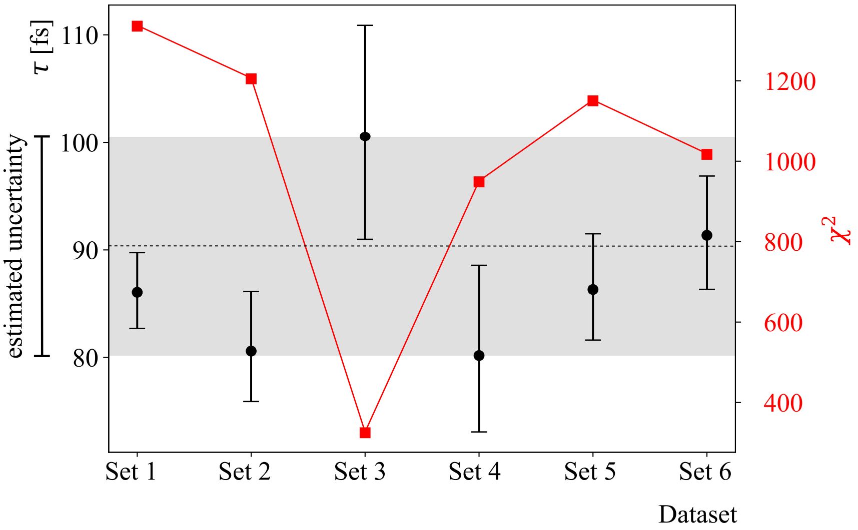

Figure 4.13: Estimation of systematic uncertainty on the lifetime $\tau$ from the TKEL selection. The $\chi^2$ gradient corresponding to the "optimal" dataset, here in blue, is shown in Figure 4.11. The remaining black-labeled points represent 5 data sets obtained by systematically gating on different TKEL spectrum ranges. The maximum difference between the data points is used as an estimation of the systematic uncertainty, corresponding to the region shaded in gray. The trend for Sets 1 to 5 is still not fully understood and necessitates additional investigation. The $\chi^2$ score obtained for each set at the minimum of the gradient is displayed in red. This provides a qualitative understanding of how well the simulation managed to reproduce the experimental data for each set, which is not accounted for in the statistical uncertainties displayed.

## 4.3 Preliminary estimation of the lifetime of the $^{35}$P $3/2^+$ state lifetime

The $^{35}$P $3/2^+_1$ state decays to the $1/2^+$ ground state by emitting a 2386 keV $\gamma$ ray. The transition is of a $E2/M1$ character, and its lifetime has not been previously reported in the literature. However, from previous measurements [36], the lifetime of the state is expected to lie within the DSAM range. In fact, the peak corresponding to the $3/2^+$ state in $^{35}$P shows a DSAM tail in the Doppler-corrected $\gamma$-ray spectra. Figure

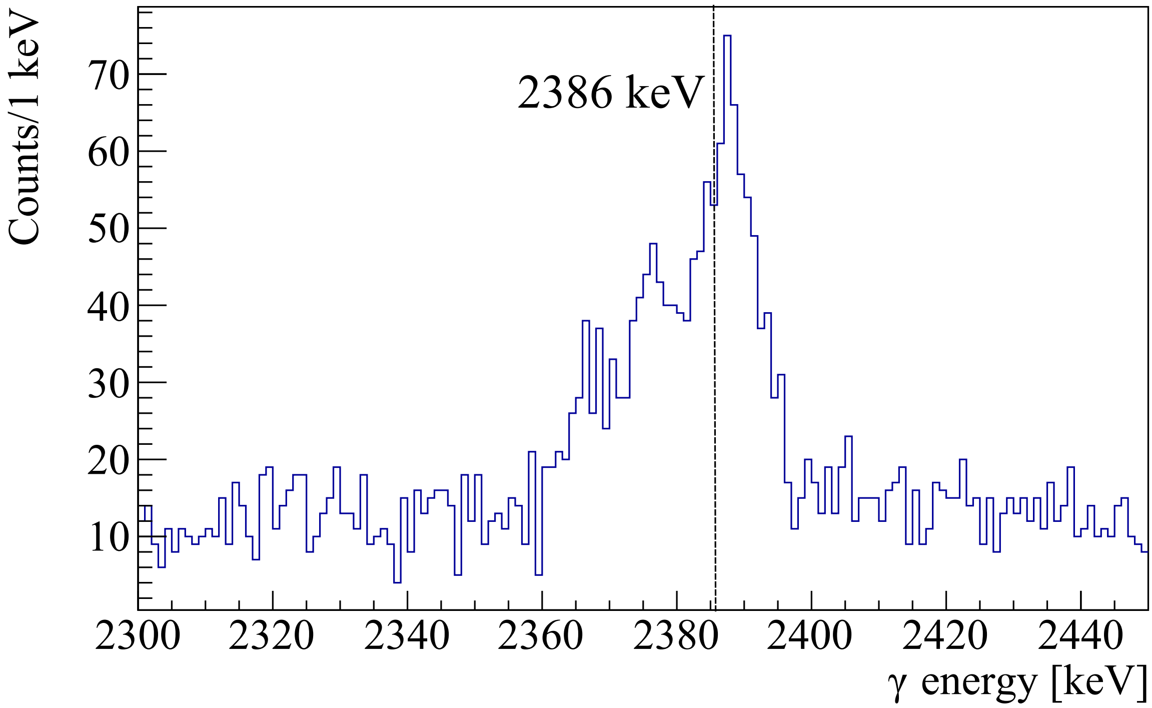

Figure 4.14: Peak corresponding to the $3/2^+_1 \rightarrow 1/2^+$ transition in $^{35}$P, expected to have an energy of 2386 keV. The DSAM tail on the left was used to estimate the lifetime of the transition via line-shape analysis.

The lifetime of the state has been extracted using the same methodology as for the $2^+_1$ state in $^{36}$S, except for the TKEL selection procedure. The gradients obtained for a set of values for the energy of the transition are shown in Figure 4.15. The global minimum is obtained for the gradient which corresponds to a transition of 2386 keV, corresponding to the real value of the transition

The analysis yielded a preliminary estimation of $\tau \sim 145(5)$ fs. The associated uncertainty was determined from the statistical uncertainty on the gradient. Nonetheless, this estimation must be further assessed by incorporating systematic effects that might affect the measurement. Notably, a possible influence from the feeding from an upper transition has not yet been investigated, and will be the subject of upcoming research.

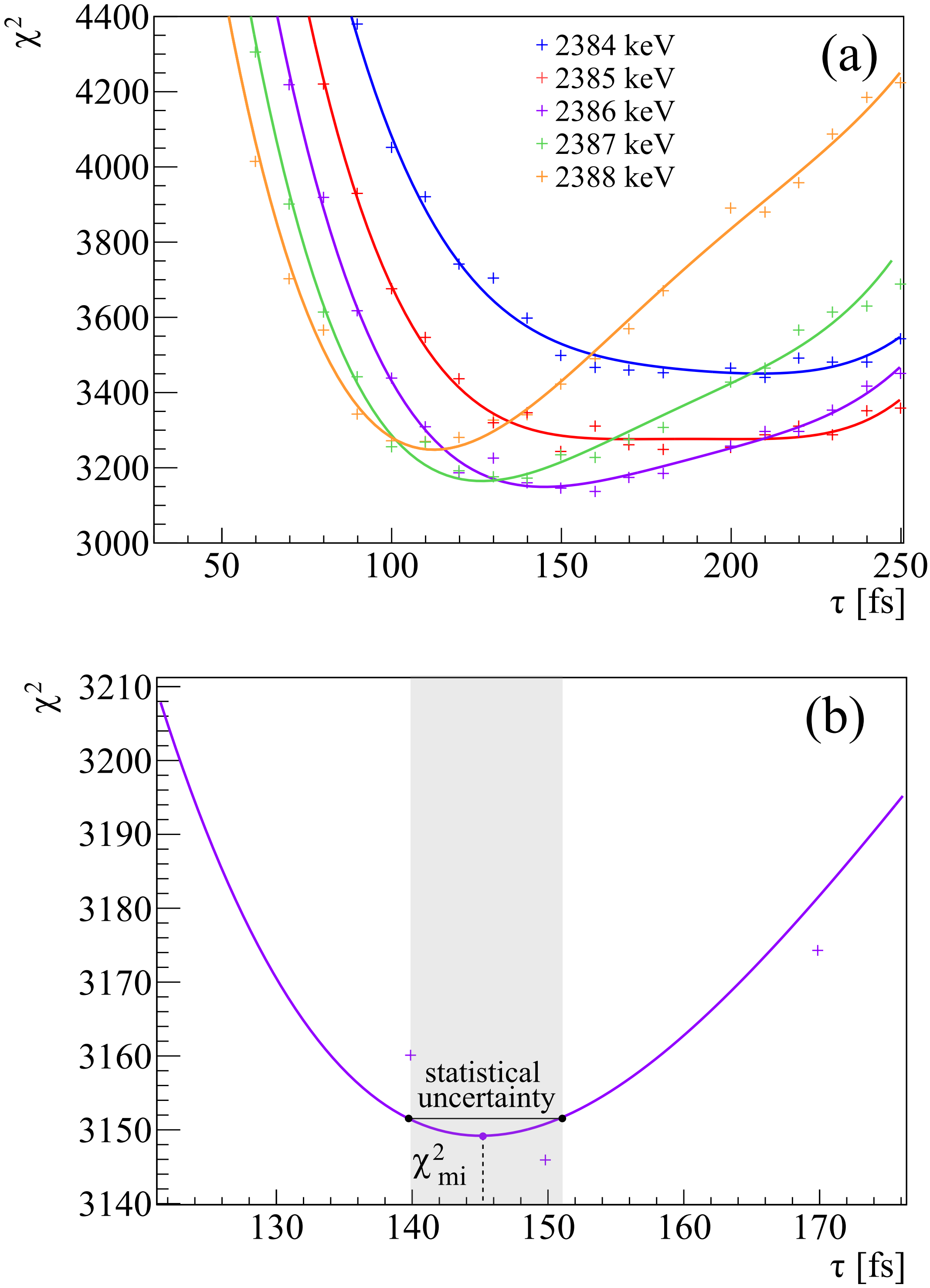

Figure 4.15: Preliminary estimation of the lifetime of the $^{35}$P $1/2^+$ state. a) Various gradients, associated with five distinct transition energies, are showcased. b) The lowest point of the fitted gradient has been identified as the estimated lifetime value. Solely considering the statistical uncertainty derived from the gradient, this yields a value of 145(5) fs. It is important to note that this estimation exclusively accounts for the statistical uncertainty, while additional factors like the influence of higher transitions' feeding have yet to be explored.

# 5

# Summary and conclusion

As one moves away from the $N = 20$ island of inversion, intruder bands commonly emerge in the excited states of nuclei in the $N = 20$ isotonic line. However, this particular excitation band remains unseen for $^{35}$P, while for $^{34}$Si discrepancies arise in the interpretation of the nature of a few of its excited states. The presence of intruder states significantly impacts various nuclear properties, such as stability and deformation. Gaining a thorough understanding of how the nuclear shell structure evolves moving away from the stability line towards the $N = 20$ island of inversion holds significant promise for refining the effective interactions needed for a comprehensive theoretical description.

This thesis provides the first-step analysis of a conducted experiment aimed at investigating the nature of a distinct set of excited states in $^{35}$P and $^{34}$Si. The central focus of the experiment was to measure the lifetimes of this particular set of states, which are predicted to lie within the range of 30 to 200 fs. The experiment, conducted at Laboratori Nazionali di Legnaro (LNL), employed the Advanced GAmma Tracking Array (AGATA) and PRISMA detectors to perform the measurement, which relied on the Doppler Shift Attenuation Method (DSAM). The technique relies on a line-shape analysis of the Doppler-shift tails present in the $\gamma$-ray spectra. These shifts result from the energy loss experienced by the recoiling ions as they traverse a degrader positioned directly after the target. To estimate the lifetimes, the experimental data is compared to a set of spectra generated by a Monte Carlo `GEANT4` simulation.

The purpose of this thesis, as outlined in Section 1.4, was to:

- analyze the experimental data gathered during the experiment (refer to Chapter 3),
- implement and optimize the Monte Carlo `GEANT4` simulation (Chapter 4),
- establish the validity of the DSAM technique by re-measuring the lifetime of the $^{36}$S $2_1^+$ state (Section 4.2)

- and, lastly, provide a preliminary estimation of the lifetime of the $3/2_1^+$ state in $^{35}$P (Section 4.3).

At present, most of the data gathered during the experimental run-time have been processed. This step involved the processing of the data acquired using the AGATA and PRISMA detectors.

The calibration process for the various detectors of PRISMA is reviewed in Section 3.1. Figure 3.5 shows the retrieved experimental mass spectra, which seem in good agreement with the results from previous experiments, reported in References [34]–[37]. The experimental mass resolution is $\Delta A/A \sim 1/70$.

As for the $\gamma$-ray spectra, the calibration of the AGATA detectors was performed based on the spectrum of $^{60}$Co and $^{152}$Eu sources. The performance of the array in terms of energy resolution was evaluated, and is discussed in Section 3.3.2. The average resolution obtained was calculated to be of $\sim 2‰$ in the $> 2$ MeV region of interest.

Furthermore, after the initial processing, the data form both detectors was merged on a time coincidence basis. The $Z$ and $A$ identification of the reaction fragments, provided by PRISMA, allowed for the analysis of the $\gamma$-ray spectra in coincidence with some specific transfer channels of interest. In particular, in this work the focus was put on the study of $^{36}$S and $^{35}$P.

The $2_1^+$ state in $^{36}$S was previously reported to have a lifetime of $\tau = 120(10)$ fs in Reference [43]. The purpose behind reevaluating the lifetime of this state was twofold: firstly, to validate the applied methodology, and secondly, to systematically identify and evaluate any challenges encountered when comparing the experimental dataset with the simulation. This specific channel was chosen due to the high amount of statistics and the observation of a $\sim$ 50 keV DSAM tail to the left the peak of interest, visible in the Doppler-corrected spectrum.

However, the initial estimations showed a significant influence of the feeding from a higher-energy transition. This higher-energy transition, namely the 902 keV $3_1^- \to 2_1^+$, has a measured lifetime of $\tau = 0.9(1)$ ps [43]. The strategy used to remove the feeding effect consisted of the selection of a specific region within the Total Kinetic Energy Loss (TKEL) spectrum where the feeding transition was minimally populated. By implementing this approach, a revised lifetime value of $\tau = 100(20)$ fs was obtained, which remains consistent with the previously reported measurement. A detailed discussion of the procedure and the uncertainty estimation is provided in Sections 4.2.2 and 4.2.4.

Moreover, the first lifetime estimation of the short-lived $3/2^+_1$ $^{35}$P was obtained, using the same procedure as for the estimation of the lifetime of the $2^+_1$ state in $^{36}$S. The estimated lifetime value is 145(5) fs, where the uncertainty is estimated as the statistical uncertainty from the $\chi^2$ gradient. Nonetheless, this is only a preliminary estimation, as systematic effects such as the feeding from higher-lying states have not yet been incorporated into the analysis. Furthermore, the uncertainty must be further assessed, and will be the subject of the upcoming work.

## 5.1 Perspective

The $\gamma$-ray spectra observed in coincidence with the $^{34}$Si and $^{35}$P ions reveal that certain $\gamma$-ray peaks exhibit a tail consistent with the DSAM broadening. This finding opens up the possibility of measuring the lifetimes of these peaks. This research has established the groundwork for such measurements by undertaking a comprehensive preparatory effort, including the processing of experimental data, the refinement of simulations, and a systematic analysis of the feeding effects that may impact such measurements.

Although our study does not provide a determination of the lifetimes of the specific states targeted by the experiment, we plan to address these transitions in future investigations, with a detailed examination of the associated feeding effects, and a rigorous estimation of measurement uncertainties. Upon obtaining the lifetime values, we will conduct a comparative analysis with theoretical calculations, to deepen our understanding of nuclear structure in the boundary of the $N = 20$ island of inversion.

# References

[1] R. Casten, *Nuclear structure from a simple perspective*, ser. Oxford studies in nuclear physics. New York: Oxford University Press, 1990, 376 pp., ISBN: 978-0-19-504599-4.

[2] E. Caurier, G. Martínez-Pinedo, F. Nowacki, A. Poves, and A. P. Zuker, "The shell model as a unified view of nuclear structure," *Reviews of Modern Physics*, vol. 77, no. 2, pp. 427–488, Jun. 16, 2005, ISSN: 0034-6861, 1539-0756. DOI: `10.1103/RevModPhys.77.427`.

[3] E. Warburton, J. Becker, and B. Brown, "Mass systematics for $A = 29 - 44$ nuclei: The deformed $A = 32$ region," *Physical Review C*, vol. 41, no. 3, 1147 – 1166, 1990, Cited by: 651. DOI: `10.1103/PhysRevC.41.1147`.

[4] K. Heyde, *Basic Ideas and Concepts in Nuclear Physics*. Institute of Physics Publishing, 1994.

[5] G. Christian, N. Frank, S. Ash, *et al.*, "Spectroscopy of neutron unbound fluorine," Ph.D. dissertation, Michigan State University, 2011.

[6] A. Poves and J. Retamosa, "The onset of deformation at the $N = 20$ neutron shell closure far from stability," *Physics Letters B*, vol. 184, no. 4, pp. 311–315, Feb. 5, 1987, ISSN: 0370-2693. DOI: `10.1016/0370-2693(87)90171-7`.

[7] N. Fukunishi, T. Otsuka, and T. Sebe, "Vanishing of the shell gap in $N = 20$ neutron-rich nuclei," *Physics Letters B*, vol. 296, no. 3, pp. 279–284, Dec. 17, 1992, ISSN: 0370-2693. DOI: `10.1016/0370-2693(92)91320-9`.

[8] Y. Utsuno, "Anomalous magnetic moment of $^{9}$C and shell quenching in exotic nuclei," *Physical Review C*, vol. 70, no. 1, p. 011 303, Jul. 14, 2004, Publisher: American Physical Society. DOI: `10.1103/PhysRevC.70.011303`.

[9] M. Salathe, H. L. Crawford, A. O. Macchiavelli, *et al.*, "Search for the $1/2^{+}$ intruder state in $^{35}$P," *Physical Review C*, vol. 102, no. 6, p. 064 317, Dec. 16, 2020, Publisher: American Physical Society. DOI: `10.1103/PhysRevC.102.064317`.

[10] T. Otsuka, M. Honma, and T. Mizusaki, "Structure of the $N = Z = 28$ closed shell studied by monte carlo shell model calculation," *Phys. Rev. Lett.*, vol. 81, pp. 1588–1591, 8 Aug. 1998. DOI: `10.1103/PhysRevLett.81.1588`.

[11] Y. Utsuno, T. Otsuka, T. Mizusaki, and M. Honma, "Varying shell gap and deformation in $N$= 20 unstable nuclei studied by the monte carlo shell model," *Physical*

*Review C*, vol. 60, no. 5, p. 054 315, Oct. 8, 1999, Publisher: American Physical Society. DOI: 10.1103/PhysRevC.60.054315.

[12] S. Khan, T. Kihm, K. Knöpfle, G. Mairle, V. Bechtold, and L. Freidrich, "The mass of $^{35}$P and spin-parity assignments for excited $^{35}$P states," *Physics Letters B*, vol. 156, no. 3, pp. 155–158, 1985, ISSN: 0370-2693. DOI: 10.1016/0370-2693(85)91499-6.

[13] R. Han, X. Q. Li, W. G. Jiang, *et al.*, "Northern boundary of the "island of inversion" and triaxiality in $^{34}$Si," *Physics Letters B*, vol. 772, pp. 529–533, Sep. 10, 2017, ISSN: 0370-2693. DOI: 10.1016/j.physletb.2017.07.007.

[14] Australian National University. (2023). "Colourful nuclide chart," [Online]. Available: https://people.physics.anu.edu.au/~ecs103/chart/ (visited on 08/31/2023).

[15] A. Poves, personal communication.

[16] IDS Collaboration, R. Lică, F. Rotaru, *et al.*, "Normal and intruder configurations in $^{34}$Si populated in the $\beta^-$ decay of $^{34}$Mg and $^{34}$Al," *Physical Review C*, vol. 100, no. 3, p. 034 306, Sep. 11, 2019, Publisher: American Physical Society. DOI: 10.1103/PhysRevC.100.034306.

[17] T. K. Alexander and J. S. Forster, "Lifetime measurements of excited nuclear levels by doppler-shift methods," in *Advances in Nuclear Physics: Volume 10*, M. Baranger and E. Vogt, Eds. Boston, MA: Springer US, 1978, pp. 197–331, ISBN: 978-1-4757-4401-9. DOI: 10.1007/978-1-4757-4401-9_3.

[18] I. Zanon, "Testing three-body forces in light nuclei: Lifetime measurements in $^{20}$O in the femtosecond range," Ph.D. dissertation, Universita degli studi di Ferrara, 2021.

[19] A. M. Stefanini, L. Corradi, G. Maron, *et al.*, "The heavy-ion magnetic spectrometer PRISMA," *Nuclear Physics A*, 5th International Conference on Radioactive Nuclear Beams, vol. 701, no. 1, pp. 217–221, Apr. 22, 2002, ISSN: 0375-9474. DOI: 10.1016/S0375-9474(01)01578-0.

[20] S. Akkoyun *et al.*, "AGATA—Advanced GAmma Tracking Array," *Nuclear Instruments and Methods in Physics Research Section A: Accelerators, Spectrometers, Detectors and Associated Equipment*, vol. 668, pp. 26–58, Mar. 11, 2012, ISSN: 0168-9002. DOI: 10.1016/j.nima.2011.11.081.

[21] INFN Padova. (2011). "The magnetic spectrometer PRISMA," [Online]. Available: https://www2.pd.infn.it/prisma/ (visited on 03/24/2023).

[22] G. Montagnoli *et al.*, "The large-area micro-channel plate entrance detector of the heavy-ion magnetic spectrometer PRISMA," *Nuclear Instruments and Methods in Physics Research Section A: Accelerators, Spectrometers, Detectors and Associated Equipment*, vol. 547, no. 2, pp. 455–463, 2005, ISSN: 0168-9002. DOI: 10.1016/j.nima.2005.03.158.

[23] S. Beghini *et al.*, “The focal plane detector of the magnetic spectrometer prisma,” *Nuclear Instruments and Methods in Physics Research Section A: Accelerators, Spectrometers, Detectors and Associated Equipment*, vol. 551, no. 2, pp. 364–374, 2005, ISSN: 0168-9002. DOI: `10.1016/j.nima.2005.06.058`.

[24] T. Mijatović *et al.*, “Response function of the magnetic spectrometer prisma for the multinucleon transfer reaction $^{40}$Ar+$^{208}$Pb,” *AIP Conference Proceedings*, vol. 1491, no. 1, pp. 346–349, 2012. DOI: `10.1063/1.4764272`.

[25] J. J. Valiente-Dobón, R. Menegazzo, A. Goasduff, *et al.*, “Conceptual design of the AGATA $2\pi$ array at LNL,” *Nuclear Instruments and Methods in Physics Research Section A: Accelerators, Spectrometers, Detectors and Associated Equipment*, vol. 1049, p. 168 040, Apr. 1, 2023, ISSN: 0168-9002. DOI: `10.1016/j.nima.2023.168040`.

[26] C. Beausang, “GRETA: the gamma-ray energy-tracking array. Status of the development and physics opportunities,” *Nuclear Instruments and Methods in Physics Research Section B: Beam Interactions with Materials and Atoms*, vol. 204, pp. 666–670, 2003, 14th International Conference on Electromagnetic Isotope Separators and Techniques Related to their Applications, ISSN: 0168-583X. DOI: `10.1016/S0168-583X(02)02148-1`.

[27] D. Bazzacco, “The Advanced GAmma ray Tracking Array AGATA,” *Nuclear Physics A*, vol. 746, pp. 248–254, 2004, Proceedings of the Sixth International Conference on Radioactive Nuclear Beams (RNB6), ISSN: 0375-9474. DOI: `10.1016/j.nuclphysa.2004.09.148`.

[28] R. M. Pérez-Vidal, “Collectivity along $N = 50$: Nuclear Structure studies on the neutron-magic nuclei $^{92}$Mo and $^{94}$Ru with AGATA and VAMOS++,” Ph.D. dissertation, Universitat de Valencia, 2019.

[29] B. Bruyneel, B. Birkenbach, and P. Reiter, “Pulse shape analysis and position determination in segmented HPGe detectors: The Agata Detector Library,” *The European Physical Journal A*, vol. 52, no. 3, 2016. DOI: `10.1140/epja/i2016-16070-9`.

[30] G. F. Knoll, *Radiation detection and measurement*, English, 2nd ed. Wiley New York, 1989, xix, 754 p. : ISBN: 0471815047.

[31] A. Lopez-Martens, K. Hauschild, A. Korichi, J. Roccaz, and J.-P. Thibaud, “$\gamma$-ray tracking algorithms: A comparison,” *Nuclear Instruments and Methods in Physics Research Section A: Accelerators, Spectrometers, Detectors and Associated Equipment*, vol. 533, no. 3, pp. 454–466, 2004, ISSN: 0168-9002. DOI: `10.1016/j.nima.2004.06.154`.

[32] F. Brandolini, N. Medina, M. De Poli, P. Pavan, M. Wilhelm, A. Dewald, and G. Pascovici, “Stopping power of Nd ions in Pb determined from $\gamma$-ray lineshape analysis in coulomb excitation,” *Nuclear Instruments and Methods in Physics Research*

*Section B: Beam Interactions with Materials and Atoms*, vol. 132, no. 1, pp. 11–17, 1997, ISSN: 0168-583X. DOI: 10.1016/S0168-583X(97)00386-8.

[33] J. Lindhard, M. Scharff, and H. E. Schioett, "RANGE CONCEPTS AND HEAVY ION RANGES (NOTES ON ATOMIC COLLISIONS, II)," *Kgl. Danske Videnskab. Selskab. Mat. Fys. Medd.*, vol. 33, no. 14, Jan. 1963.

[34] R. Chapman, Z. M. Wang, M. Bouhelal, *et al.*, "Particle-core coupling in $^{37}$S," *Physical Review C*, vol. 93, no. 4, p. 044 318, Apr. 18, 2016, ISSN: 2469-9985, 2469-9993. DOI: 10.1103/PhysRevC.93.044318.

[35] R. Chapman, A. Hodsdon, M. Bouhelal, *et al.*, "Spectroscopy of neutron-rich $^{34,35,36,37,38}$P populated in binary grazing reactions," *Physical Review C*, vol. 92, no. 4, p. 044 308, Oct. 9, 2015, Publisher: American Physical Society. DOI: 10.1103/PhysRevC.92.044308.

[36] L. Grocutt, R. Chapman, M. Bouhelal, *et al.*, "Lifetime measurements of $N \approx$ 20 phosphorus isotopes using the AGATA $\gamma$-ray tracking spectrometer," *Physical Review C*, vol. 100, no. 6, p. 064 308, Dec. 13, 2019, Publisher: American Physical Society. DOI: 10.1103/PhysRevC.100.064308.

[37] L. Grocutt, R. Chapman, M. Bouhelal, *et al.*, "Lifetime measurements of states of 35S, 36S, 37S, and 38S using the agata $\gamma$-ray tracking spectrometer," *Phys. Rev. C*, vol. 106, p. 024 314, 2 2022. DOI: 10.1103/PhysRevC.106.024314.

[38] AGATA Data Analysis Team. (2019). "AGATA Data Analysis User's guide for Local Level Processing," [Online]. Available: https://atrium.in2p3.fr/nuxeo/nxfile/default/878272cd-bb33-4b35-aa30-227c1a38e8d1/blobholder:0/AGATA_LLP_UsersGuide.pdf (visited on 08/22/2023).

[39] AGATA Data Analysis Team. (2018). "AGATA Data Analysis User's guide for Global Level Processing," [Online]. Available: https://atrium.in2p3.fr/nuxeo/nxfile/default/addab6d3-ef22-453a-a3b1-629f145376f3/blobholder:0/AGATA_GLP_UsersGuide.pdf (visited on 08/22/2023).

[40] K. L. Wang, J. G. Wang, X. H. Zhou, *et al.*, "Lifetime measurement of the first excited state in $^{37}$S," *Phys. Rev. C*, vol. 94, p. 044 316, 4 Oct. 2016. DOI: 10.1103/PhysRevC.94.044316.

[41] E. Farnea, F. Recchia, D. Bazzacco, T. Kröll, Z. Podolyák, B. Quintana, and A. Gadea, "Conceptual design and monte carlo simulations of the agata array," *Nuclear Instruments and Methods in Physics Research Section A: Accelerators, Spectrometers, Detectors and Associated Equipment*, vol. 621, no. 1, pp. 331–343, 2010, ISSN: 0168-9002. DOI: https://doi.org/10.1016/j.nima.2010.04.043.

[42] S. Agostinelli *et al.*, "Geant4— a simulation toolkit," *Nuclear Instruments and Methods in Physics Research Section A: Accelerators, Spectrometers, Detectors and Associated Equipment*, vol. 506, no. 3, pp. 250–303, 2003, ISSN: 0168-9002. DOI: https://doi.org/10.1016/S0168-9002(03)01368-8.

[43] K.-H. Speidel, S. Schielke, J. Leske, *et al.*, “First g-factor measurements on semi-magic $^{36}$S and their implications for the rigidity of the $N = 20$ shell closure,” *Physics Letters B*, vol. 659, no. 1, pp. 101–106, 2008, ISSN: 0370-2693. DOI: 10.1016/j.physletb.2007.11.049.

[44] R. L. Workman *et al.*, “Review of Particle Physics,” *PTEP*, vol. 2022, p. 083C01, 2022. DOI: 10.1093/ptep/ptac097.

[45] P. Young, *Everything You Wanted to Know About Data Analysis and Fitting but Were Afraid to Ask*. Springer Briefs in Physics, 2015, ISBN: 978-3-319-19050-1.

# List of Figures

# List of Tables

# List of Acronyms

**IPM** Independent Particle Model

**AGATA** Advanced GAmma Tracking Array

**DSAM** Doppler Shift Attenuation Method

**HPGe** High-Purity Germanium

**IC** Ionization Chamber

**LNL** Laboratori Nazionali di Legnaro

**MCP** Micro-Channel-Plate

**MWPPAC** Multi-wire Parallel-Plate Avalanche Counter

**PSA** Pulse Shape Analysis

**ToF** Time-of-Flight

**FWHM** Full Width Half Maximum

**TKEL** Total Kinetic Energy Loss